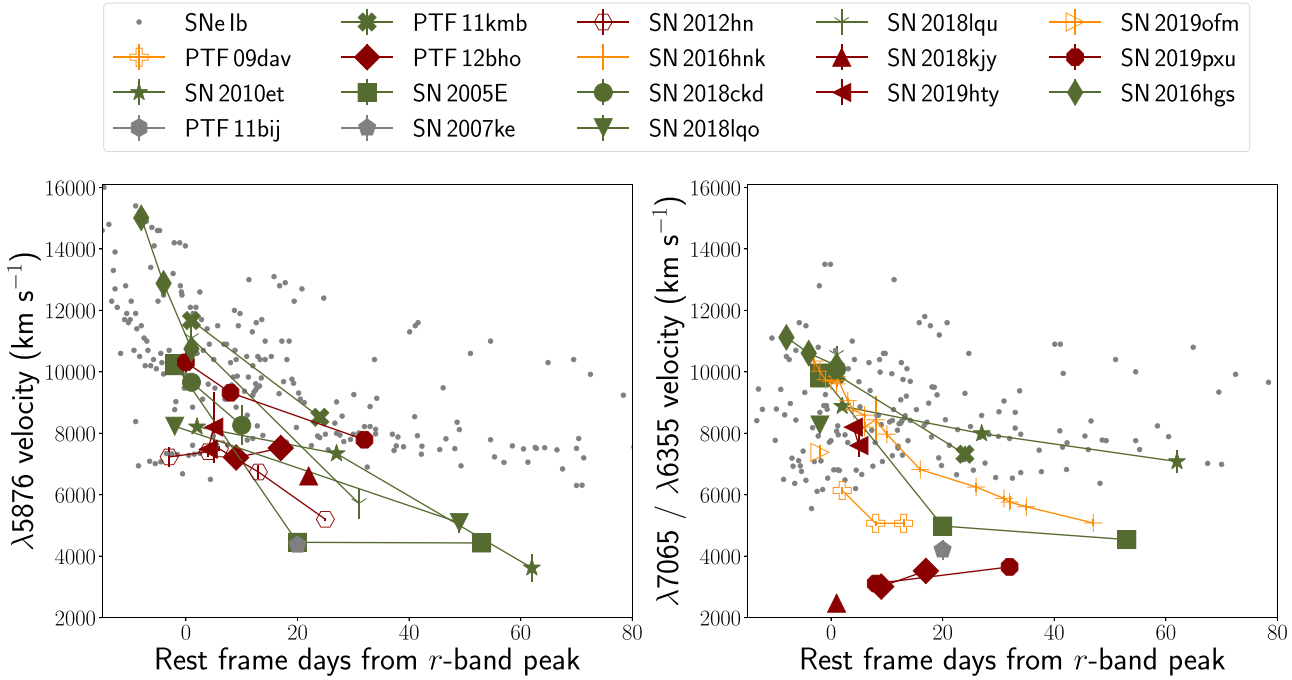

Figure 10. Evolution of photospheric line velocity as a function of phase from the r-band peak for the combined sample of Ca-rich gap transients discussed in this paper. Points joined by solid lines represent the velocity evolution for the same object. We also plot the velocity evolution of the respective lines observed in normal SNe Ib in the sample of Liu et al. (2016), as gray dots in the background. Individual events are shown by markers as indicated in the legend, with their marker colors indicating whether they belong to the Ca-Ib/c class with green (shown in dark green) or red (shown in red) continua, or to the Ca-Ia class (shown in orange). The left panel shows the velocity evolution of the prominent He I λ5876 line in cases where it is unambiguously identified (with solid symbols), or the likely nearby Na I feature (for SN 2012hn in hollow symbols). The right panel shows the velocity evolution of the He I λ7065 feature for the Ca-Ib/c events and the Si II λ6355 feature for the Ca-Ia events.

is a relatively nearby event at 30 Mpc, our nebular-phase spectral sequence extends out to ≈235 days, showing that [Ca II] emission continues to dominate the spectrum from the earliest to these very late phases and hence the Ca-rich classification is independent of the exact phase of the nebular spectrum. We note that the events with red continua SN 2012hn, SN 2018kjy, and SN 2018gwo exhibit relatively stronger [O I] lines relative to [Ca II], when compared with other objects observed at similar phases. SN 2012hn and SN 2018gwo are also notable for exhibiting clear signatures of Fe-group elements around 4000–6000 Å similar to the late-time spectra of subluminous SNe Ia.

3.2.2. The Ca-Ia Class

Figure 8 shows the nebular-phase spectra for the Ca-Ia objects, which are dominated by [Ca II] lines. It is important to note the difference between the Ca-Ia objects and the class of 1991bg-like objects in the nebular phase—while the 1991bg-like objects exhibit strong features of Fe-group elements in the blue part of the spectrum in the nebular phase, the Ca-Ia objects show nearly no signatures of such features in the blue-side spectra at similar phases. We demonstrate this by plotting a nebular-phase spectrum of the 1991bg-like object SN 2005ke (Silverman et al. 2012) in Figure 8. SN 2005ke also exhibits a strong emission feature at 7290 Å near [Ca II]; however this feature could be associated with [Fe II] and [Ni II] emission given the strong Fe-group elements observed in the blue side of the spectrum (Flörs et al. 2020; see also Polin et al. 2019b who suggest that this feature is due to [Ca II]). Unlike the Ca-Ib/c objects, the Ca-Ia objects exhibit very weak or no [O I] emission in the nebular phase. The nebular-phase spectrum of SN 2016hnk (Galbany et al. 2019) exhibits a narrow double-peaked feature at the [Ca II] line, and is noticeably narrower than those of other objects.[32] However this could be due to the very late phase of the spectrum—unavailable for the other, fainter objects in this class.

3.2.3. [Ca II]/[O I] Ratio

In the nebular-phase spectra of the combined sample of events, we fit a Gaussian to the [Ca II] and [O I] emission features to estimate their flux ratio. We compute the fluxes by fitting a single Gaussian (see, e.g., Jerkstrand 2017) to the respective line emission features. We do not compute the absolute flux in these lines as spectro-photometric calibration is not available for several spectra in the literature.[33] Instead, we compute the [Ca II]/[O I] ratio for each spectrum. For several late-time spectra [O I] is barely or not detected. In such cases, we compute an upper limit on the [O I] flux by using the rms of the flux around the expected position of the line center to compute a 1σ upper limit on the [O I] flux assuming that the [Ca II] and [O I] lines have the same velocity width (this provides a lower limit on the [Ca II]/[O I] ratio). We estimate the uncertainties in the line ratios by computing the standard deviations in these quantities from 1000 Monte Carlo realizations of the spectra, where the samples are created by adding flux uncertainties in the same way as with the photospheric-phase spectra. Table 3 lists the best-fit parameters

[32] However, the late-time spectrum of SN 2016hnk reported by Jacobson-Galán et al. (2020) does not show a clear double peak.
[33] Absolute calibration would also require contemporaneous photometry, which is largely unavailable.

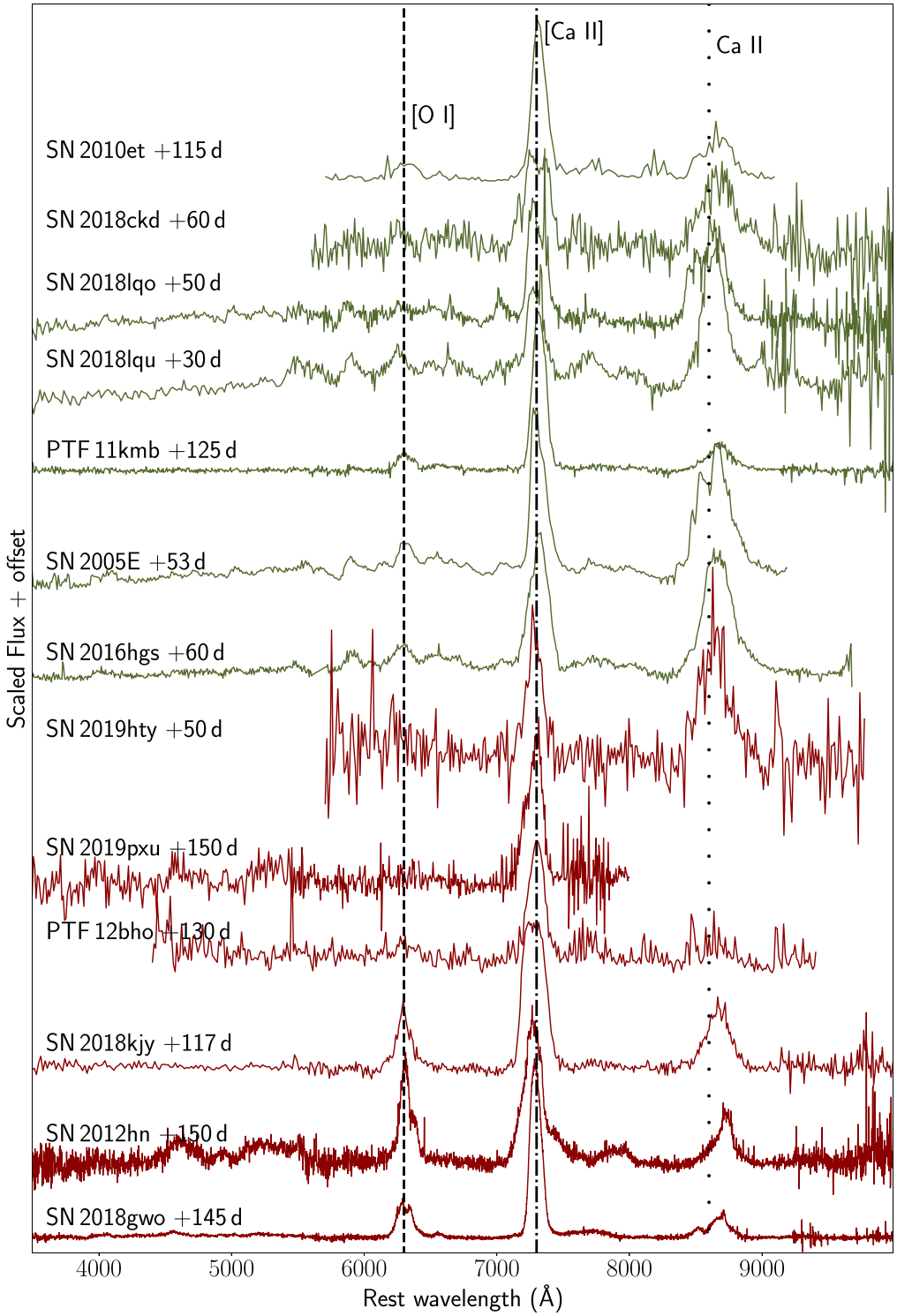

Figure 11. Nebular-phase spectra of the Ca-Ib/c events in the ZTF sample combined with the same for events in the literature. The transient name and phase of the spectrum are indicated next to each spectrum. The color coding of the spectra is the same as that in Figure 6. The prominent nebular lines of [O I], [Ca II], and Ca II are marked.

for the sample of events in this paper as well as for all published spectra in the literature.

We plot the evolution of the [Ca II]/[O I] ratio in these sources compared to a sample of nebular-phase spectra of other types of stripped-envelope SNe in ZTF in Figure 12. These spectra were obtained either as a part of confirmation spectra for candidate Ca-rich gap transients identified from photometry or as a part of nebular-phase follow-up of a volume-limited sample of stripped-envelope SNe (C. Fremling et al. 2020, in preparation). The Ca-rich gap transients occupy a unique phase space in this plot with high [Ca II]/[O I] at all phases in their evolution. We also show the threshold of [Ca II]/[O I] = 2 used to select the sample of Ca-rich gap transients in this paper, which clearly separates out the Ca-rich events from the normal events, which primarily occupy a phase space of [Ca II]/[O I] $\lesssim$ 1 at all phases. We note that several of the red Ca-Ib/c events exhibit relatively low [Ca II]/[O I] at all phases, where the [Ca II]/[O I] values are smaller by a factor of $\approx$2 than those

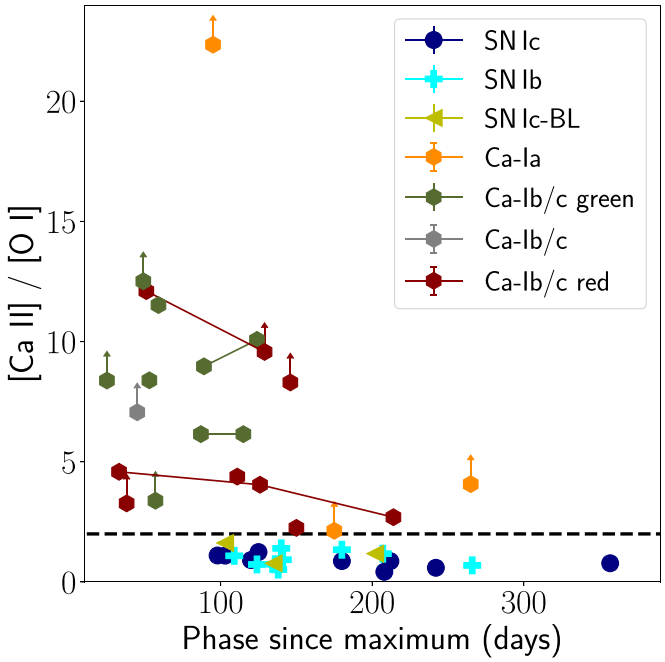

Figure 12. [Ca II]/[O I] ratio for the Ca-rich gap transients and stripped-envelope SNe in the ZTF volume-limited experiment. The black horizontal dashed line shows the [Ca II]/[O I] ratio defined as the threshold in this paper for classification as a Ca-rich transient. Symbols with upward arrows indicate lower limits on the [Ca II]/[O I] ratio where the [O I] feature is not detected with statistical significance. The Ca-rich events are indicated by hexagons with colors that reflect their peak light spectroscopic appearance as discussed in the text.

of the green Ca-Ib/c events. This trend is consistent with the qualitative analysis in Section 3 where we note stronger [O I] features in the red events. The [Ca II]/[O I] estimates result in lower limits for all the Ca-Ia events, suggesting that [O I] is not detected in the nebular-phase spectra of these objects.

3.3. Photometric Evolution

In Figure 13, we compare the *r*-band light curves of the ZTF sample of Ca-rich gap transients near peak light, to four characteristic light curves of the literature Ca-rich events PTF 09dav (Sullivan et al. 2011), PTF 10iuv (Kasliwal et al. 2012), PTF 12bho (Lunnan et al. 2017), and SN 2016hgs (De et al. 2018a). The comparison sample is chosen to encompass the diversity of the photospheric-phase spectral properties reported in the literature sample. The *r*-band light curves of the full ZTF sample are largely similar to those of the comparison sample, with the exception of SN 2019ofm and SN 2019pxu, which exhibit more luminous and broader light curves than the comparison objects. SN 2018lqo exhibits a prominent early-time "bump" of ≈1 mag as compared to the light curve of SN 2010et. Excess emission is also marginally detected in the light curve of SN 2018kjy, although at much lower significance.

In the bottom right panel of Figure 13, we show a zoomed-in image of the early *r*-band light curves of SN 2018lqo and SN 2018kjy together with that of SN 2016hgs, which was previously reported as a peculiar Ca-rich gap transient with a prominent double-peaked light curve. For comparison, we plot the well-sampled light curve of SN 2010et, which shows a purely monotonic rise in its early light curve, as is found for all the other events in the full sample. The early excess emission in the light curve of SN 2018lqo is similar in luminosity and timescale to the early emission in SN 2016hgs. Early excess in SN 2018kjy is detected but is of lower significance, and hence we do not discuss it further here. SN 2018gwo has no ZTF coverage near peak light, although the peak light photometry published on the TNS and the late-time decay tail are consistent with the literature sample of events if we assume that the source was first detected ≈7 days before peak light. We caution, however, that we are unable to measure the time of peak or any other light-curve parameter for this object due to the absence of photometry around peak.

3.3.1. Light-curve Parameters

We fit the light curve of each transient (in every filter available) around peak light (within 20 days of peak) with a low-order polynomial (order of 3 to 4) and derive parameters describing the light-curve peak and timescale. We perform the same fitting for all multi-color photometry data available for the literature sample of Ca-rich gap transients. We use the functional fits to determine the times of peak in each filter, the peak apparent and absolute magnitudes (m_p and M_p respectively), and the characteristic rise time and decline time. We define the rise and decay time ($t_{r,\,1/2}$ and $t_{f,\,1/2}$) of the light curve as the time it takes to rise or decline to half flux from peak light. In addition, we compute the characteristic decay of the light curve (in magnitudes) in 7 days from peak light, denoted by Δm_7.

We estimate uncertainties on these quantities by Monte Carlo sampling of the derived parameters from 1000 realizations of each light curve using the photometric uncertainties of each point in the light curve. We restrict our fitting to photometric bands that have at least one data point before peak light, since it is not possible to estimate the peak magnitude without a corresponding detection before peak. In addition, for sources that do not have photometry sampling the relevant time period of the rise or fall of the light curve, we do not compute the respective Δm_7, rise time, or fall time. For SN 2018gwo, photometry is not available around peak light, and hence we use the reported photometry near peak on the TNS (Wiggins 2018) as a lower limit on the peak magnitude. In computing the peak apparent and absolute magnitude, we also correct the photometry of the literature events for Galactic extinction using the maps of Schlafly & Finkbeiner (2011) and the extinction law of Cardelli et al. (1989) with $R_V = 3.1$.

We do not correct for any additional host galaxy extinction due to the absence of Na I D absorption in their spectra and the remote locations of these events. The only exception is SN 2012hn, for which we assume a host extinction of $E(B-V) = 0.2$ mag, which was estimated from Na I D absorption in its spectra (Valenti et al. 2014). The best-fit parameters from the light-curve fitting are given in Table 5.

3.3.2. Color Evolution

Figure 14 shows the $g-r$ and $r-i$ color evolution of the complete sample of Ca-rich gap transients discussed in this paper. For comparison to other types of SNe, we also show the well-sampled color curves of the nearby SN Ia 2011fe (Nugent et al. 2011) and the SN Ib iPTF 13bvn (Cao et al. 2013). Ca-rich gap transients redden rapidly in $g-r$ color compared to SNe Ia, although the color evolution has a trend similar to that of the SN Ib iPTF 13bvn. However, all the Ca-rich gap transients are redder than iPTF 13bvn in $g-r$ at similar epochs. The same trend is also seen in the $r-i$ color evolution. The $g-r$ evolution of both the Ca-Ib/c objects

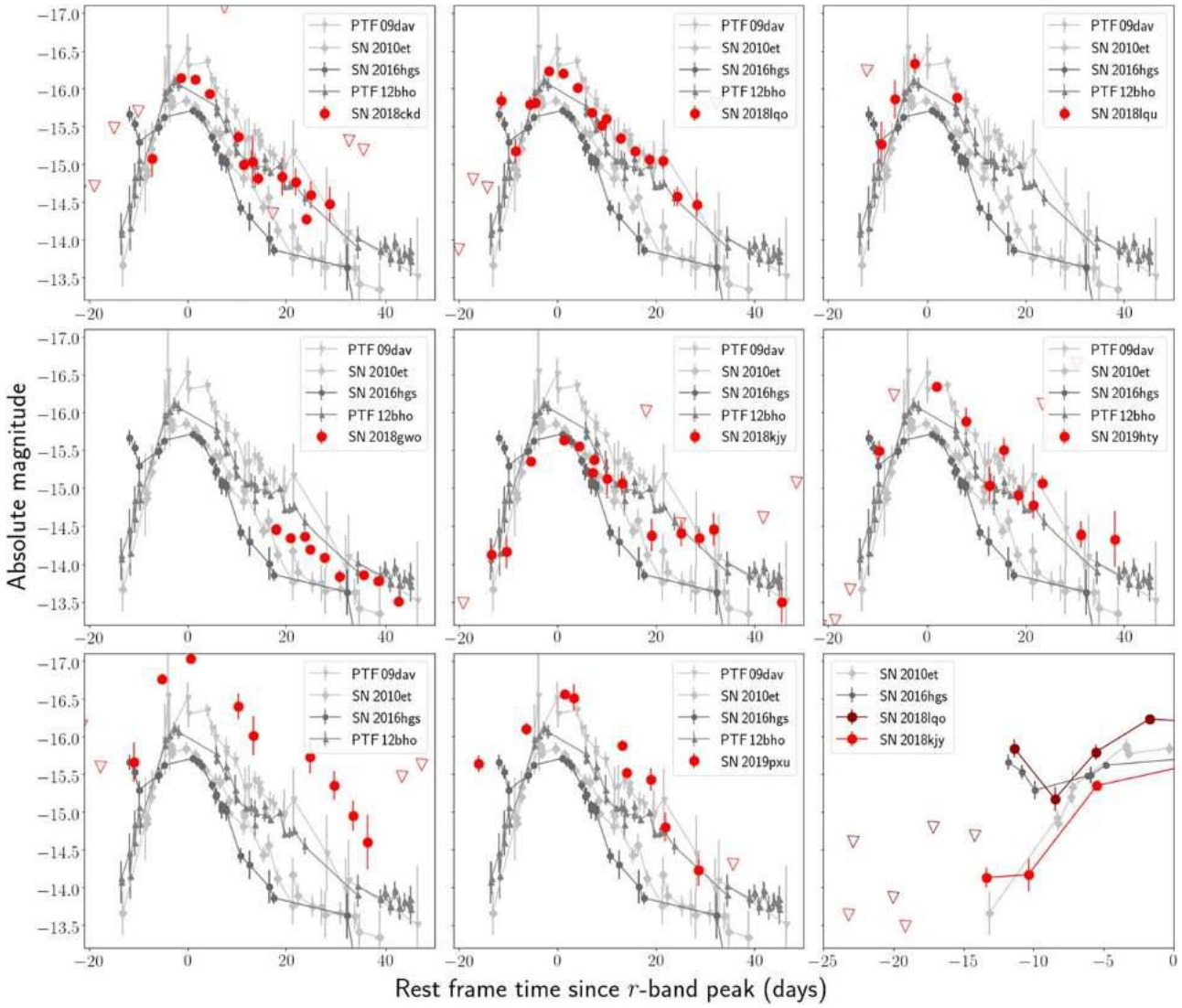

Figure 13. Comparison of the *r*-band evolution of this sample of Ca-rich gap transients to some previously confirmed events—PTF 09dav (Sullivan et al. 2006), SN 2010et (Kasliwal et al. 2012), PTF 12bho (Lunnan et al. 2017), and SN 2016hgs (De et al. 2018a). In each panel, the *r*-band photometry for the ZTF sample is presented as red points while the archival sources are plotted in shades of gray. The photometric evolution is shown as a function of rest-frame time from the best estimate of the *r*-band peak (except in the case of SN 2018gwo; see text). Inverted triangles denote 5σ upper limits. Bottom right panel: Comparison of the early-time bumps seen in the light curves of some of the transients in the ZTF Ca-rich sample to those of the literature events SN 2016hgs (which exhibits an early-time bump; De et al. 2018a) and SN 2010et (which exhibits a monotonic rise; Kasliwal et al. 2012).

with red continua and the Ca-Ia objects is systematically redder than that of the Ca-Ib/c objects with green continua, consistent with the suppressed blue flux in the spectra of the former objects. We note that the complete sample of Ca-rich gap transients occupies a narrow distribution around $g - r \approx 0.7$ mag near peak light, which we later use to simulate their light curves for estimation of volumetric rates from the ZTF survey (Section 5).

3.3.3. Luminosity, Width, and Color Relationship

In Figure 15, we plot the peak *r*-band magnitude of the transients as a function of the decline in *r* band in 7 days from peak (Δm_7) and the time taken to fall to half the maximum flux ($t_{f,1/2}$). While some objects have well-sampled light curves on the rise to estimate the time taken to rise from half-maximum flux to maximum, the majority of literature events do not have well-constrained pre-peak light curves and hence we only plot the fall time from peak. We choose the *r* band as it is the most commonly available filter for the combined photometric sample and allows us to perform a homogeneous analysis on the largest number of objects. For comparison of this phase space to the general trend followed by thermonuclear SNe, we plot the same parameters for SNe Ia. We use the sample of ZTF SN Ia light curves published in Yao et al. (2019), and compute the same quantities using the fitting techniques mentioned above with the *r*-band light curves. The distribution of these SNe Ia shows the expected luminosity–width relationship (the Phillips relation; Phillips 1993) with more luminous events being systematically slower-evolving.[34] In order to investigate the presence of a luminosity–width relationship in the full sample

[34] Note that the canonical relationship for SNe Ia is defined using the magnitude decline in 15 days after peak in the *B* band versus peak absolute magnitude M_B. However, we choose to conduct this analysis on Δm_7 against peak absolute magnitude in the *r* band M_r since the faint and fast-declining Ca-rich gap transients usually lack photometry extending beyond ≈15 days from maximum.

Table 5
Light-curve Fit Parameters for the Sample of Ca-rich Gap Transients Presented in This Paper, together with the Fits for the Literature Sample of Ca-rich Gap Transients

Object	Filter	t_p MJD	m_p	M_p	$t_{r,\,1/2}$ (days)	$t_{f,\,1/2}$ (days)	Δm_7 (mag)	References
SN 2018ckd	*r*	58277.67 ± 0.33	18.95 ± 0.02	−16.17	6.20 ± 0.29	8.68 ± 0.54	0.54 ± 0.04	This work
SN 2018ckd	*g*	58274.21 ± 1.31	19.69 ± 0.07	−15.43	⋯	10.17 ± 1.78	0.33 ± 0.19	This work
SN 2018ckd	*i*	58280.67 ± 0.66	19.00 ± 0.08	−16.12	7.88 ± 0.60	12.60 ± 1.07	0.33 ± 0.05	This work
SN 2018lqo	*r*	58351.92 ± 0.23	19.62 ± 0.02	−16.21	7.33 ± 0.25	10.47 ± 0.50	0.41 ± 0.02	This work
SN 2018lqo	*g*	58349.97 ± 0.35	20.09 ± 0.05	−15.73	5.80 ± 0.27	7.67 ± 0.41	0.64 ± 0.06	This work
SN 2018lqo	*i*	58353.41 ± 1.85	19.49 ± 0.17	−16.33	7.69 ± 1.76	11.04 ± 1.49	0.37 ± 0.14	This work
SN 2018lqu	*r*	58370.83 ± 2.27	19.57 ± 0.30	−16.44	7.40 ± 1.37	⋯	⋯	This work
SN 2018kjy	*r*	58460.93 ± 0.33	18.85 ± 0.06	−15.63	⋯	12.36 ± 1.49	0.31 ± 0.06	This work
SN 2018kjy	*g*	58458.18 ± 1.81	19.81 ± 0.25	−14.68	⋯	⋯	0.64 ± 0.46	This work
SN 2019hty	*r*	58657.90 ± 0.83	18.63 ± 0.05	−16.38	8.81 ± 0.78	11.55 ± 0.76	0.33 ± 0.04	This work
SN 2019hty	*g*	58653.44 ± 0.68	19.01 ± 0.08	−16.00	⋯	8.05 ± 0.84	0.59 ± 0.12	This work
SN 2019ofm	*r*	58723.58 ± 1.02	18.60 ± 0.04	−17.03	8.39 ± 1.14	11.07 ± 1.16	0.34 ± 0.06	This work
SN 2019ofm	*g*	58721.71 ± 1.65	19.69 ± 0.11	−15.94	⋯	⋯	⋯	This work
SN 2019pxu	*r*	58747.78 ± 0.48	18.90 ± 0.04	−16.56	⋯	11.83 ± 0.57	0.30 ± 0.03	This work
SN2005E	*B*	53387.15 ± 0.35	18.14 ± 0.13	−14.52	⋯	5.06 ± 1.26	⋯	[1]
SN2005E	*V*	53387.15 ± 0.51	17.51 ± 0.07	−15.15	⋯	7.93 ± 0.89	0.62 ± 0.12	[1]
SN2005E	*R*	53388.72 ± 0.71	17.13 ± 0.05	−15.53	⋯	8.90 ± 1.25	0.55 ± 0.12	[1]
SN2005E	*I*	53389.51 ± 1.32	16.73 ± 0.07	−15.93	⋯	⋯	0.39 ± 0.14	[1]
SN2007ke	*R*	54369.54 ± 1.82	17.77 ± 0.06	−16.59	⋯	10.29 ± 1.73	0.33 ± 0.14	[1]
PTF 09dav	*r*	55054.38 ± 0.78	19.86 ± 0.09	−16.22	6.26 ± 0.63	9.28 ± 1.00	0.49 ± 0.08	[2]
SN 2010et	*r*	55359.36 ± 0.25	19.03 ± 0.03	−15.69	6.30 ± 0.32	9.62 ± 0.55	0.49 ± 0.03	[3]
SN 2010et	*g*	55357.04 ± 0.39	19.56 ± 0.08	−15.15	⋯	8.01 ± 0.95	0.61 ± 0.11	[3]
SN 2010et	*i*	55361.86 ± 0.73	18.90 ± 0.04	−15.82	⋯	⋯	0.32 ± 0.05	[3]
PTF 11bij	*r*	55635.44 ± 1.60	20.28 ± 0.10	−15.68	⋯	9.46 ± 2.40	0.45 ± 0.22	[3]
SN2012hn	*B*	56031.06 ± 0.48	18.72 ± 0.06	−13.42	⋯	7.44 ± 1.02	0.69 ± 0.12	[4]
SN2012hn	*V*	56031.60 ± 0.63	17.15 ± 0.03	−14.99	⋯	⋯	0.32 ± 0.05	[4]
SN2012hn	*R*	56031.06 ± 0.84	16.59 ± 0.02	−15.55	⋯	15.23 ± 1.00	0.14 ± 0.05	[4]
SN2012hn	*r*'	56035.62 ± 2.94	16.90 ± 0.11	−15.24	⋯	11.74 ± 3.01	0.26 ± 0.21	[4]
SN2012hn	*I*	56037.90 ± 3.17	16.22 ± 0.01	−15.92	⋯	9.01 ± 3.17	0.40 ± 0.20	[4]
SN2012hn	*G*	56031.01 ± 0.80	17.45 ± 0.17	−14.69	⋯	9.31 ± 2.22	0.47 ± 0.27	[4]
SN2012hn	*g*'	56031.01 ± 0.83	17.45 ± 0.16	−14.69	⋯	9.31 ± 2.13	0.47 ± 0.24	[4]
PTF 11kmb	*r*	55800.73 ± 0.34	18.79 ± 0.01	−15.57	⋯	11.35 ± 0.42	0.28 ± 0.02	[5]
PTF 11kmb	*g*	55797.95 ± 1.01	19.37 ± 0.03	−14.99	⋯	10.41 ± 1.13	0.36 ± 0.09	[5]
PTF 12bho	*r*	55992.00 ± 0.25	18.99 ± 0.03	−16.04	6.97 ± 0.27	10.29 ± 0.35	0.42 ± 0.02	[5]
SN 2016hgs	*r*	57691.80 ± 0.24	18.91 ± 0.03	−15.45	⋯	9.43 ± 0.38	0.42 ± 0.03	[6]
SN 2016hgs	*g*	57683.22 ± 1.00	19.48 ± 0.10	−14.88	⋯	13.29 ± 0.98	0.25 ± 0.10	[6]
SN 2016hgs	*i*	57692.85 ± 0.21	18.54 ± 0.03	−15.82	⋯	9.47 ± 0.34	0.44 ± 0.03	[6]
SN2016hnk	*B*	57691.35 ± 0.60	18.92 ± 0.05	−15.31	⋯	7.00 ± 0.62	0.75 ± 0.09	[7]
SN2016hnk	*V*	57691.74 ± 0.74	17.46 ± 0.03	−16.77	⋯	⋯	0.39 ± 0.08	[7]
SN2016hnk	*r*	57692.78 ± 0.43	17.18 ± 0.02	−17.05	⋯	12.78 ± 0.62	0.32 ± 0.03	[7]
SN2016hnk	*i*	57691.34 ± 0.78	17.34 ± 0.03	−16.89	⋯	⋯	0.27 ± 0.06	[7]
SN2016hnk	*z*	57697.79 ± 2.42	17.38 ± 0.07	−16.85	⋯	⋯	0.09 ± 0.06	[7]
SN2016hnk	*g*	57695.27*	18.53 ± 0.04	−15.70	⋯	6.47 ± 2.25	0.76 ± 0.10	[7]

Note. t_p denotes the time of peak in the respective filter, m_p denotes the peak apparent magnitude (corrected for Galactic extinction using the maps of Schlafly & Finkbeiner (2011)), M_p denotes the peak absolute magnitude, $t_{r,\,1/2}$ denotes the rise time to peak from half of the peak flux, and $t_{f,\,1/2}$ denotes the fall time from peak to half the peak flux. Δm_7 denotes the drop in magnitude from the time of peak to 7 days after peak. Photometry for some of the sources in the literature was obtained from the Open Supernova Catalog (Guillochon et al. 2017). The data were originally published in [1] Perets et al. (2010), [2] Sullivan et al. (2011), [3] Kasliwal et al. (2012), [4] Valenti et al. (2014), [5] Lunnan et al. (2017), [6] De et al. (2018a), and [7] Galbany et al. (2019).

(This table is available in its entirety in machine-readable form.)

of Ca-rich objects, we compute the Spearman correlation coefficient between the two pairs of plotted parameters and find no significant evidence of correlation. The corresponding correlation coefficients are 0.25 between M_p and Δm_7 (p-value of 0.35) and −0.36 between M_p and $t_{f,\,1/2}$ (p-value of 0.18), suggesting no statistically significant correlation between these parameters.

We now examine possible differences in the photometric properties between the Ca-Ib/c and the Ca-Ia objects. Due to the absence of peak light spectroscopy for SN 2007ke and PTF 11bij, we are unable to ascertain the nature of the blue continuum at peak light; however, their early nebular-phase spectra show lines characteristic of SNe Ib/c suggesting their membership in the class of Ca-Ib/c objects. The peak luminosity distributions of green and red events among the Ca-Ib/c objects are consistent with each other; however, the Ca-Ia objects are typically more luminous. The total number of events remains too small for us to draw a conclusion on the statistical significance of the differences. Specifically, we note that the Ca-Ib/c events with red continua exhibit systematically

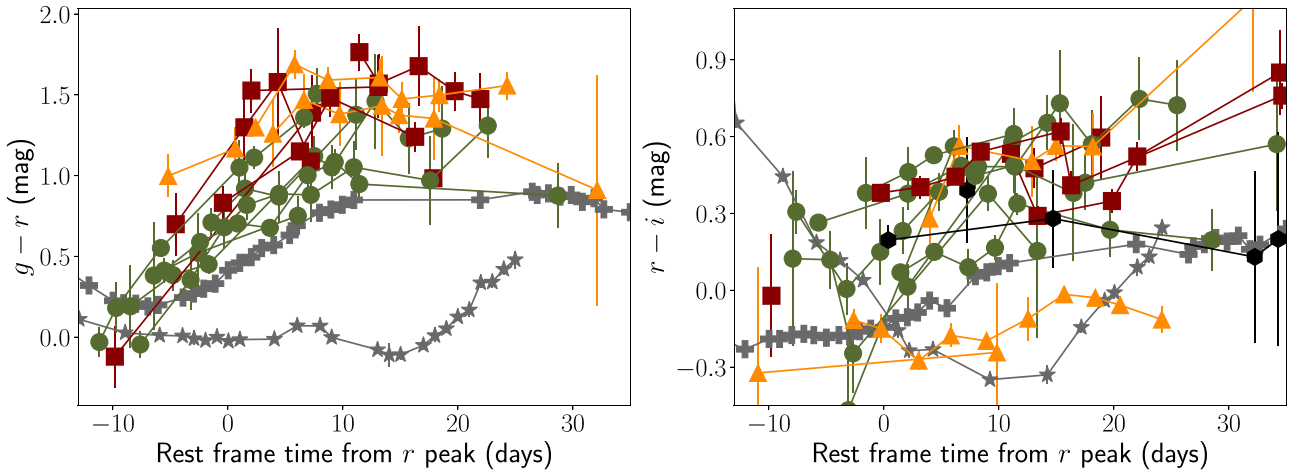

Figure 14. Comparison of the $g - r$ and $r - i$ color curves of the sample of known Ca-rich gap transients, color-coded by their spectroscopic membership in the green Ca-Ib/c (green circles), red Ca-Ib/c (red squares), or Ca-Ia (orange triangles) class. For comparison, we also show the color evolution curves of the Type Ia SN 2011fe (Nugent et al. 2011) as dark gray stars and the Type Ib iPTF 13bvn (Cao et al. 2013) as dark gray crosses, which are systematically bluer in $g - r$ than the Ca-rich gap transients at similar epochs. Events in the combined sample without a peak light spectrum are shown as black circles.

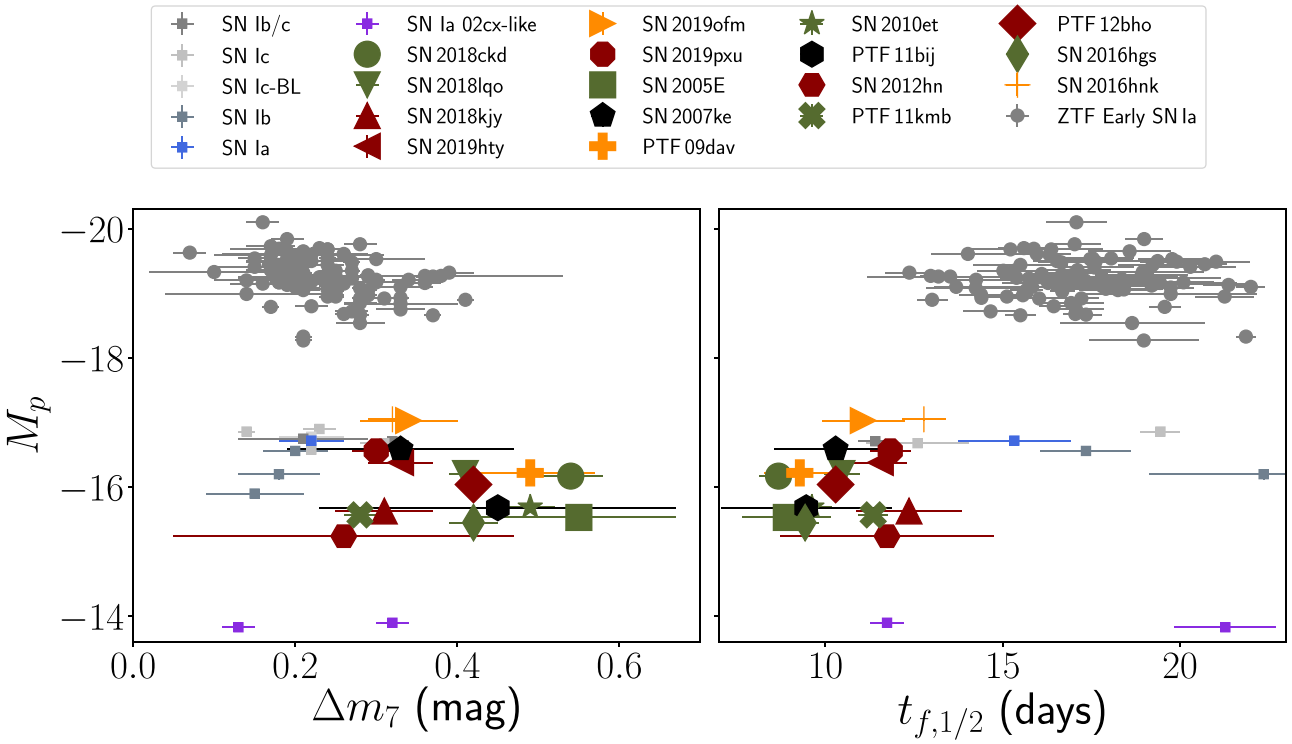

Figure 15. Luminosity–width phase space for the r-band light curves of Ca-rich gap transients (symbols are shown with the object names in the legend). The individual events are colored by their spectral type at peak light. Green Ca-Ib/c events are indicated by green and those with reddened continua are indicated by red. Ca-Ia events are indicated in orange and the marker symbols for all events are indicated in the legend. We are unable to constrain the peak light spectroscopic properties of SN 2007ke and PTF 11bij, and hence show these objects in black. For comparison, we plot the same phase space of timescales for the ZTF 2018 early SN Ia sample in Yao et al. (2019) as gray dots, together with the same parameters for objects in the control sample (squares; indicated in the legend by their spectroscopic type at peak).

slower light curves than the Ca-Ib/c events with green continua, as shown by their smaller Δm_7 and larger $t_{f,1/2}$ values. A two-sample Kolmogorov–Smirnov (K-S) test suggests that the null hypothesis probability that the two sets of values are drawn from the same underlying population is $<5\%$ for $t_{f,1/2}$ and $<18\%$ for Δm_7. While this is only marginally significant due to the small number of events, we further examine this trend in Figure 16.

We show the dependence of Δm_7 as a function of the $g - r$ color of the transient near peak light in Figure 16. The $g - r$ photometric colors at peak light are not available for several events in the combined sample, and hence we use both the spectro-photometric colors derived from peak light spectroscopy and the photometric colors where available. Since the photometric colors are not always available at the same phase as the spectroscopy, there are differences between the derived photometric and spectro-photometric colors. The Ca-Ib/c events separate into two classes of events based on their $g - r$ colors, while the Ca-Ia events exhibit colors intermediate between the two classes but redder than the green Ca-Ib/c

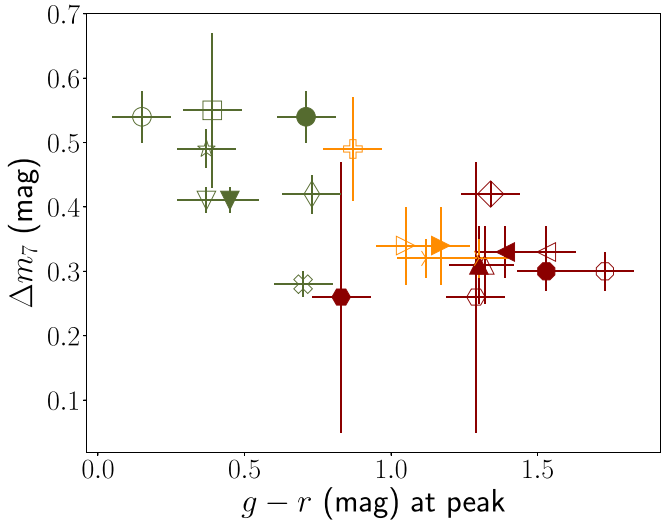

Figure 16. Dependence of the rate of light-curve evolution post-peak in the r band (Δm_7) on the transient $g-r$ color at peak. The symbol color coding and markers are the same as those used in Figure 15. Hollow symbols indicate colors computed from spectro-photometry on observed spectra within ≈10 days of peak light, while solid symbols indicate colors derived from peak light photometry where available. The colors have been corrected for foreground Galactic extinction.

events. Specifically, we note that the Ca-Ib/c events with bluer $g-r$ colors at peak exhibit larger Δm_7 (faster photometric evolution) at peak, while the red Ca-Ib/c events are slower-evolving, consistent with the trend observed in Figure 15. However, we caution against drawing conclusions about any correlations between these two parameters as the photometric and spectro-photometric colors are not available at the same phase in all cases. We find that the green and red events in the Ca-Ib/c sample are separated at $g-r \approx 1$ mag at peak light; the Ca-Ia objects also exhibit redder colors of $g-r > 1$ mag at peak, consistent with their line-blanketed spectra.

3.3.4. Dependence on Spectroscopic Properties

In Figure 17, we plot the photospheric velocity at peak light against the peak r-band magnitude of the sources to examine the dependence of the photospheric-phase velocity on the peak luminosity of each event. In the case of SN 2018kjy, we are unable to measure the He line velocities directly due to the large number of narrow lines, and hence we estimate typical line velocities in the spectra from the P-Cygni absorption velocities of ≈4000 km s^{-1}. We do not find a clear dependence of the photospheric-phase velocity on the peak luminosity of the events, but note that the events with green continua have higher photospheric-phase velocities than the red events.

The right panel of Figure 17 shows the dependence of the peak light photospheric velocity on the rate of decay of the light curve, Δm_7. As per the formalism for radioactively powered light curves laid down in Arnett (1982), the peak light photospheric velocity and light-curve evolution near peak are indicators of the ejecta mass in the explosion. We thus also plot lines of constant ejecta mass in the right panel to guide the eye to the range of ejecta masses in the sample. We construct these lines by creating analytic light curves using the formalism of Arnett (1982) assuming two constant opacities of $\kappa = 0.07$ cm^2 g^{-1} (as relevant for SNe Ib/c; Cano 2013; Taddia et al. 2018) and $\kappa = 0.2$ cm^2 g^{-1} (relevant for completely ionized hydrogen-free material). We caution, however, that the Arnett diffusion model has several assumptions which may not be satisfied in these explosions (see Khatami & Kasen 2019 for a review). We do not find a dependence of the peak photospheric velocity on the light-curve evolution near peak. It is important to note that the inferred ejecta masses can vary significantly depending on the assumed opacity. The majority of Ca-Ib/c events with green continua lie on the contours of lower ejecta masses (between 0.1 and 0.4 $M_\odot$), while the red Ca-Ib/c and Ca-Ia events lie near larger ejecta masses (up to ≈1 $M_\odot$ for $\kappa = 0.07$ cm^2 g^{-1}, but <0.5 $M_\odot$ for $\kappa = 0.2$ cm^2 g^{-1}). However, we stress that redder events also likely have higher effective optical opacity in the ejecta than their green counterparts, as evident from the strong suppression of flux in the blue, which would suggest increased bound–bound opacity from Fe-group material. As such, this effect would decrease the ejecta masses inferred from assuming a constant opacity across all events.

3.3.5. Late-time Photometric Evolution

In Figure 4, we show the late-time (>40 days after r-band peak) photometric evolution of the sample of Ca-rich gap transients presented in this paper together with published photometry of events in the literature. While most of the late-time photometry presented here was obtained using targeted follow-up observations using P60 + SEDM, P200 + WaSP, and Keck I + LRIS, we also stack several epochs (over up to 30 days) of the high-cadence ZTF observations to derive flux limits at late times. Owing to its small distance, SN 2018gwo has good photometric follow-up from ZTF up to ≈100 days from the estimated peak time. We also show a numerically computed Arnett model (Arnett 1982) for the decline rate expected from a radioactively powered light curve with ejecta mass of 0.5 $M_\odot$ and ^{56}Ni mass of 0.015 $M_\odot$. The model parameters are chosen based on the typical values found in previous studies (Perets et al. 2010; Kasliwal et al. 2012; Valenti et al. 2014; De et al. 2018a).

Compared to the expected ^{56}Ni decay tail shown in Figure 4, the luminosity at late times is much fainter than the prediction from the Arnett model, while the decay slope is also steeper for these events. The characteristics are consistent with the fast-rising light curves of these events, which suggest low ejecta masses and incomplete γ-ray trapping at late times. Figure 4 also shows the last deep photometric limits obtained using P200 and Keck for this sample of events, extending out to ≈1.5 years after peak light. Although SN 2018gwo is detected with Keck (owing to its small distance) out to ≈500 days after peak light, the very late-time follow-up photometry for all the objects could be potentially contaminated by underlying host systems. We discuss the presence of potential underlying host stellar systems from late-time imaging in Section 4.

4. Locations and Host Environments

Here, we examine the environments and host properties of the Ca-rich gap transients analyzed in our sample. The host environments of the literature sample of transients have been noted in several works previously for their preference for old environments located far away from their host galaxies, with no evidence of parent stellar populations at the location of the transients (Perets et al. 2010, 2011; Kasliwal et al. 2012; Yuan et al. 2013; Lyman et al. 2014, 2016; Mulchaey et al. 2014;

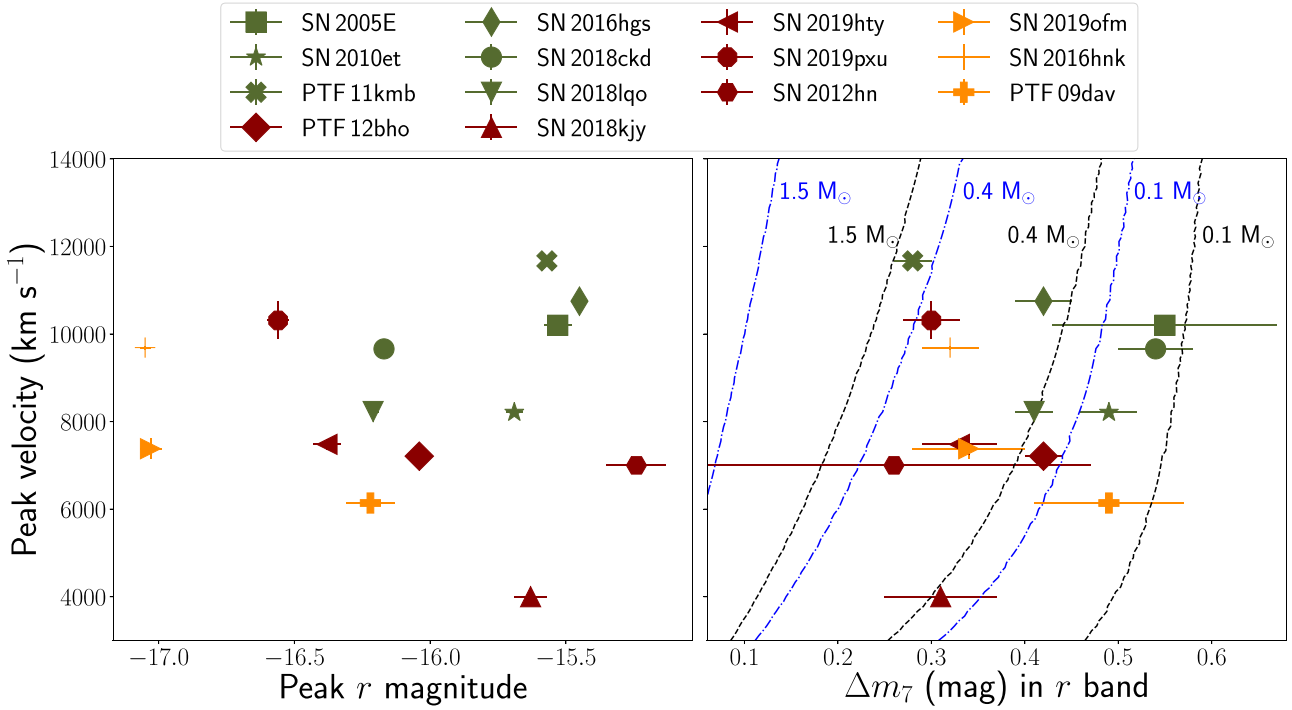

Figure 17. Photospheric-phase line velocities as a function of the light-curve peak luminosity (in the r band) and the timescale of evolution (characterized by Δm_7) for the sample of Ca-rich gap transients analyzed in this paper. We use the velocity of the He I λ5876 feature from the spectrum taken closest to the estimated time of peak light in the r band (if available within 10 days of peak) for the Ca-Ib/c objects, and the Si II λ6355 velocity for the Ca-Ia objects. The left panel shows the peak velocity as a function of the peak r-band magnitude and the right panel shows the peak velocity as a function of Δm_7. The right panel also shows the contours of the constant ejecta mass computed using the analytical model of Arnett (1982) to guide the eye on the range of ejecta masses found in the sample. We show the ejecta mass contours for two different optical opacities of $\kappa = 0.07$ cm^2 g^{-1} (black dashed lines) and $\kappa = 0.2$ cm^2 g^{-1} (blue dotted–dashed lines).

Lunnan et al. 2017; De et al. 2018a; Shen et al. 2019). Additionally, Yuan et al. (2013) found that the offset distribution of a subset of events in the literature sample is inconsistent with the stellar mass profiles of their host galaxies, while Yuan et al. (2013) and Shen et al. (2019) show that their offset distributions are consistent with globular clusters or old metal-poor stellar populations. Frohmaier et al. (2018) show that the preference for large host offsets in the PTF sample cannot be explained by the reduced recovery efficiency on top of bright galaxies. However, all of these works are based on heterogeneous samples of events gathered from different surveys with diverse selection effects that are difficult to quantify. As this is the first unbiased systematic experiment to classify a large sample of Ca-rich gap transients, we perform a systematic analysis of their locations and host environments.

4.1. Host Galaxy Morphology

We begin with analyzing the host galaxy morphologies of these events. Our selection criteria for these events did not include any restrictions on the host galaxy type. Six out of the eight events in this sample were found in S0/E early-type host galaxies (four out of the eight were in E-type galaxies), and all of the events were found at projected galactocentric offsets > 6 kpc. Two events (SN 2019ofm and SN 2019pxu) were found in late-type galaxies, although at relatively large host offsets (11 and 17.5 kpc respectively, corresponding to host-normalized offsets of 2.1 and 4.5 R_e[35]). Notably, both the Ca-Ia objects SN 2016hnk and SN 2019ofm were found in late-type star-forming galaxies, while PTF 09dav was found to be hostless in late-time imaging and the nearest galaxy with a known redshift was a star-forming spiral $\approx$40 kpc from the transient location. However, we caution that PTF 09dav is close to several faint extended sources (see Figure 3 in Kasliwal et al. 2012), which could be nearby dwarf galaxies; it also shows Hα emission in its latest nebular-phase spectrum, although it could be associated with circumstellar photoionized gas around the SN (Kasliwal et al. 2012).

Nevertheless, the preference of these transients for old host environments with large offsets is striking as compared to other types of transients in the local universe. The preference for early-type galaxies in this sample is reminiscent of that observed for 91bg-like SNe Ia (Howell 2001; Neill et al. 2009; Perets et al. 2010; Taubenberger 2017), although the preference of Ca-rich gap transients for early-type galaxies is more extreme than that for these events. A total of 19 91bg-like SNe Ia were classified in the CLU experiment in the span of time considered in this paper, out of which 10 events were found in early-type galaxies while the rest were in late-type galaxies. The near-equal distribution in early- and late-type galaxies for 91bg-like SNe Ia is consistent with the stellar mass distribution between early-type and late-type galaxies in the local universe (Kochanek et al. 2001; Bell et al. 2003).

4.2. Locations and Offset Distribution

In Figure 18, we compare the host offset distribution of the ZTF Ca-rich gap transients (both in physical projected distance and in host-normalized distance) to that of other types of SNe in the volume-limited experiment—SNe Ia, SNe II, and SNe Ib/c. The host offsets for each event in the sample are computed from the host galaxy in the CLU catalog, which is

[35] R_e is defined as the half-light radius of the apparent host galaxy.

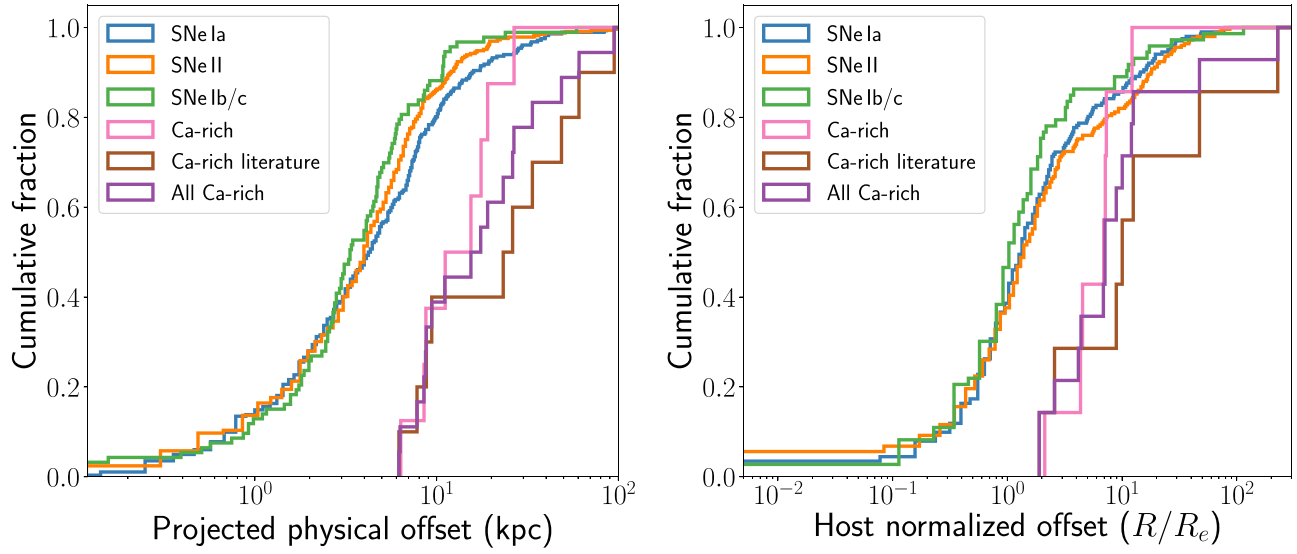

Figure 18. Projected offset distribution of all transients in the CLU experiment. The left panel shows the distribution in units of physical projected distance (kpc), while the right panel shows the distribution in host offset normalized by the half-light Petrosian radius of the host galaxy. The half-light Petrosian radii are derived from the SDSS (Abolfathi et al. 2018) catalog, and hence are limited to transients occurring in the SDSS footprint.

confirmed to be at the same redshift as the SN. As shown in Figure 18, SNe Ib/c show systematically smaller physical offsets than SNe II, while SNe II show systematically smaller offsets than SNe Ia. However, the Ca-rich gap transients exhibit a significantly skewed distribution of larger offsets (in terms of both physical offsets and host-normalized offsets) than any of the object types in the comparison sample.

Using a two-sample K-S test, we can rule out the possibility that the entire population of SNe Ia and Ca-rich gap transients in the ZTF sample originates from the same underlying population at 99.9% confidence. For comparison, we also show the host offset distribution of the literature sample of Ca-rich gap transients and the total combined sample of Ca-rich gap transients, whose distribution appears to extend out to larger galactocentric offsets. A K-S test between the ZTF and literature samples of offsets does not indicate a statistically significant difference between the two distributions (p-value of 0.28); however, the limitation of the CLU experiment to finding transients within 100″ of their host galaxies prevents us from finding objects with very large host offsets. The consistent offset distributions justify the use of the full sample of offset distributions to estimate the incompleteness of the CLU sample (Section 5).

Several previous works have suggested that the lack of Ca-rich gap transients at small host offsets may be due to their faint light curves, which would make them difficult to detect on top of high surface brightness regions on galaxies (Foley 2015). Frohmaier et al. (2017) presented the recovery efficiency for the PTF pipeline as a function of the source magnitude and local surface brightness, demonstrating that the recovery efficiency is indeed lower in regions of high surface brightness. Yet, Frohmaier et al. (2018) showed that the preference of the small PTF sample of Ca-rich gap transients for large host offsets cannot be explained by the reduced recovery efficiency on bright galaxy backgrounds.

While the recovery efficiency for the ZTF pipeline is currently not available, we can empirically examine if the offset locations for the faint Ca-rich gap transients in the ZTF sample can be primarily explained by poor recovery efficiency on the cores of galaxies. In Figure 19, we show the projected offset

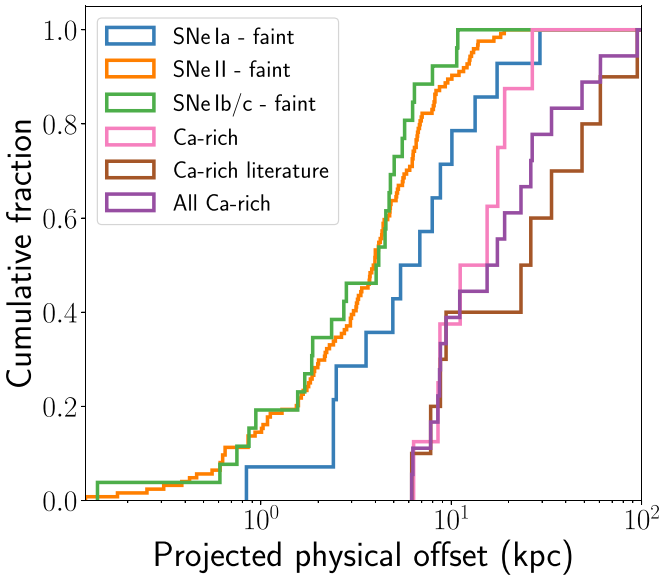

Figure 19. Projected offset distribution of all faint transients that were detected at $M > -17$ in the CLU experiment.

distribution of all transients fainter than $M = -17$ mag in the CLU experiment. The offset distribution of the SNe II, SNe Ib/c, and SNe Ia in this low-luminosity sample extends from the smallest offsets at <1 kpc to ≈30 kpc. Notably the Ca-rich gap transients continue to stand out with large host offsets of at least 5 kpc (extending out to ≈40 kpc). The skewed offset distribution of Ca-rich gap transients even in this sample of low-luminosity transients suggests that the low recovery efficiency of faint transients cannot completely explain the remote locations of these events.

We further compare the environments of 91bg-like SNe Ia to those of the Ca-rich gap transients. We plot the projected offset distributions of all SNe Ia, 91bg-like SNe Ia, and Ca-rich gap transients in Figure 20. We also show the simulated radial distribution of globular clusters from Shen et al. (2019) for two different Sérsic indices. The literature sample analyzed in this

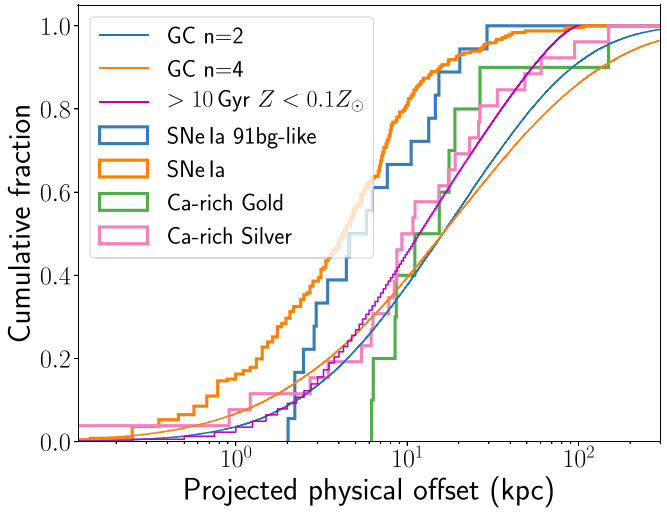

Figure 20. Offset distribution comparison of the "gold" and "silver" samples of Ca-rich gap transients discussed in this paper to those of all SNe Ia and 91bg-like SNe Ia in the volume-limited experiment. Our gold sample includes the literature sample of events (which includes the gold sample discussed in Shen et al. 2019 in addition to the Ca-Ia objects discussed in this work) and the ZTF sample, while the silver sample includes the silver sample discussed in Shen et al. (2019) in addition to the ZTF sample of events. We also show the simulated offset distribution of globular clusters for two Sérsic indices, as well as the offset distribution for old (>10 Gyr), metal-poor ($Z < 0.1\ Z_\odot$) stars discussed in Shen et al. (2019).

paper includes Ca-Ia events from the literature, in addition to the "gold" sample in Shen et al. (2019). Thus, in plotting the radial offset distribution of the sample of Ca-rich events, we define our new "gold" sample by adding the ZTF sample of events to the literature sample (including all the Ca-Ia objects, amounting to a total of 18 events).

We also define a new "silver" sample by adding the ZTF sample of events to the silver sample in Shen et al. (2019), which included Ca-rich events without photometric constraints at peak light (amounting to a total of 24 events). 91bg-like SNe Ia show systematically smaller offsets than the Ca-rich gap transients in this sample, and systematically larger offsets than the full population of SNe Ia. A two-sample K-S test between the offset distributions of SN 91bg–like SNe Ia and the gold and silver samples of Ca-rich gap transients produces null hypothesis probabilities of being drawn from the same underlying population at <2.5% and <10% respectively. We conclude that the discrepancies between the environments of 91bg-like and Ca-rich events suggest that stellar mass alone does not dictate the rates of Ca-rich gap transients. Long delay times and/or low metallicities in these remote environments of early-type galaxies have thus been suggested to play an important role (Perets et al. 2010; Yuan et al. 2013; Meng & Han 2015; Shen et al. 2019).

In addition to being skewed toward larger offsets compared to SNe Ia, the Ca-rich gold and silver samples exhibit offset distributions different from those of globular clusters and old metal-poor stars from IllustrisTNG simulations (Marinacci et al. 2018; Naiman et al. 2018; Nelson et al. 2019). Specifically, the gold sample distribution is skewed toward larger offsets than these two populations. However, the silver sample offset distribution is more consistent with both these distributions (consistent with the result in Yuan et al. 2013 and Shen et al. 2019), although there are discrepancies at relatively large offsets. Notably, all of the Ca-rich gap transients found in this experiment are in "rich" environments with $\gtrsim$10 galaxies clustered near the nominal host, while Shen et al. (2019) found that 17% of globular cluster hosts are in rich clusters (see Section 4.3).

We examine deep late-time images of the locations of these transients to investigate if there is any evidence for underlying stellar populations at these locations. We show these images in Figure 21. SN 2018ckd shows clear evidence of a relatively bright pointlike source (marked with a yellow circle) offset by <1 kpc from the transient location. This source is also detected in archival imaging of the field in the Dark Energy Camera Legacy Survey's Data Release 8 (Dey et al. 2019) at a magnitude of $r \approx 23.5$ mag and $g - r \approx 0.3$ mag, corresponding to an absolute magnitude of ≈ -11.5 mag if at the redshift of the transient. However, the source is unlikely to be a globular cluster as it is more luminous than nearly the entire known luminosity function of globular clusters (Harris 1996). We orient the slit to include the extended galaxy $\approx 10''$ to the north of SN 2018ckd (marked with a yellow circle) during nebular-phase spectroscopy, and find it to be an unrelated background galaxy at $z = 0.1$, consistent with the photometric redshift of the object in SDSS.

An extended source is detected near the location of SN 2018lqu (marked with a yellow circle), although its redshift is unknown. If at the redshift of the transient, its magnitude of $r \approx 21.4$ would imply an absolute magnitude of $M_r \approx -14.5$ mag similar to a dwarf galaxy's. SN 2018lqo, SN 2018gwo, and SN 2019hty show evidence of faint and extended sources underneath their locations, which likely contaminate our photometry measurements during very late-time imaging (Figure 21). However, we caution that the density of unrelated background sources at the depths of the late-time images ($\approx$25 mag) is high (Hogg et al. 1997). Using the methodology of Bloom et al. (2002), we find that the chance coincidence probability of an unrelated $\approx$25 mag galaxy within a $5''$ radius of the transient is $\sim$50%, while the same for a $10''$ radius is $\sim$95%. Thus, the association of these sources to the transients can only be determined from deep spectroscopy in the future. SN 2018kjy is notable for the smallest host offset ($\approx$6 kpc) in the ZTF sample, and is located within the halo of its host galaxy. SN 2019ofm is found on top of its spiral host galaxy, while SN 2019pxu is at a large offset from its spiral host and has a point source (marked with a yellow circle) within $5''$ of its location ($M_r \approx -12.1$ mag if at the redshift of the transient). The latest Keck images of SN 2019ofm and SN 2019pxu still show the transient clearly. Future deep imaging for these events will help disentangle the potential host contamination in our latest photometry measurements, as well as allow inspection of potential underlying hosts.

4.3. Group and Cluster Environments

Given the large host offsets of the Ca-rich gap transient sample, we analyze the environments of the assumed host galaxies to check if they are part of a larger group or cluster that may explain the remote locations of these transients. Mulchaey et al. (2014), Lunnan et al. (2017), and De et al. (2018a) performed a similar analysis on the literature sample of Ca-rich gap transients, and demonstrated that these objects prefer host galaxies in groups and clusters. For each transient, we construct a sample of nearby galaxies by selecting galaxies from the CLU catalog (with a previously known spectroscopic redshift) within

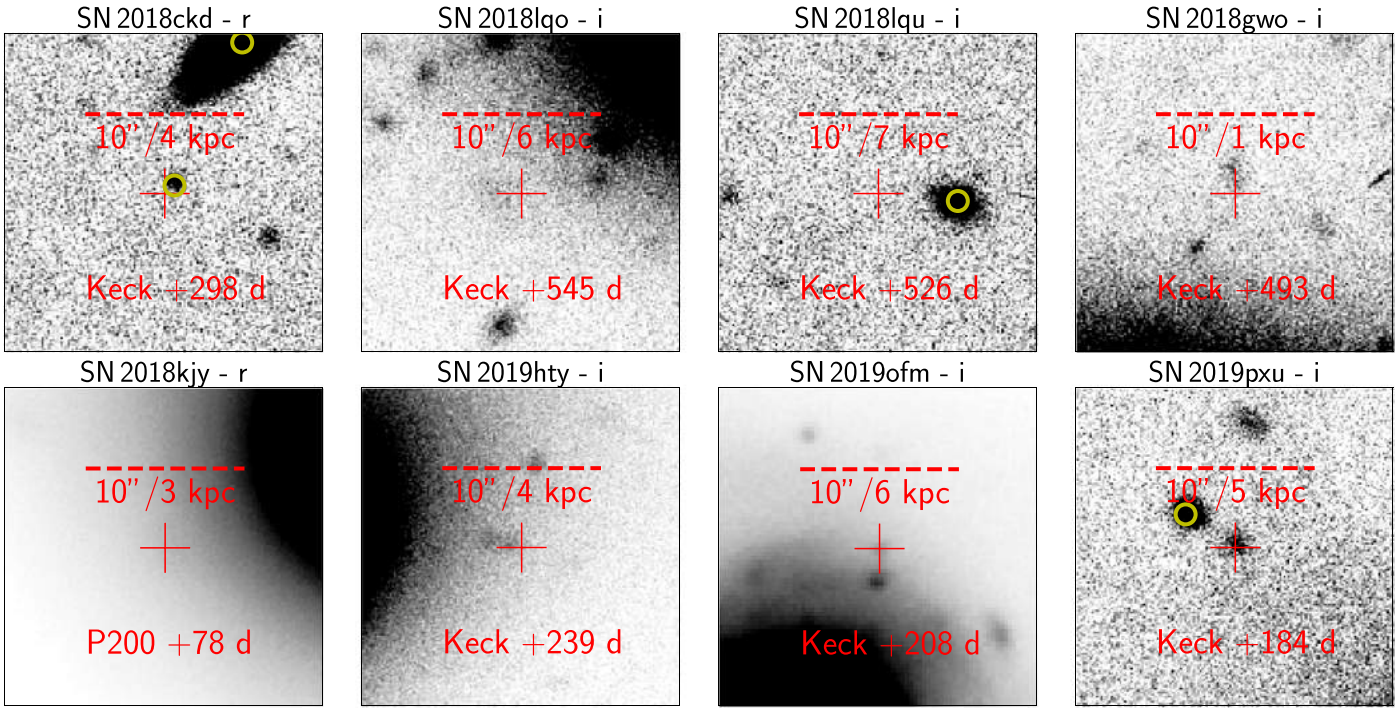

Figure 21. Cutouts of the locations of the Ca-rich gap transients presented in this paper from late-time ground-based imaging of the transient locations. North is up and east is left in each cutout. The source name, filter and phase of observation, instrument used, and physical scale of the image at the redshift of the transient are shown in each panel. The crosses show the location of the transient. Yellow circles mark the locations of potential host systems also detected in pre-explosion archival imaging (see text).

a projected radius of 1 Mpc and a recession velocity difference of ± 3000 km s^{-1} from the location of the transient.

We emphasize that since galaxy catalogs are highly incomplete at the redshifts of these transients (Kulkarni et al. 2018; Fremling et al. 2019), these distributions are only lower limits to the true number of galaxies in the environments of these transients. We show the velocity histograms of the identified galaxies in Figure 22. As shown, the environments of the Ca-rich gap transient host galaxies are largely dominated by groups and clusters with at least 10 known objects within the selection criteria defined above. SN 2018lqo is in the densest environment with 87 known nearby galaxies. We thus conclude that all of the transients in the ZTF sample are in group or cluster environments, consistent with that reported for the literature sample presented in Lunnan et al. (2017) and De et al. (2018a).

5. Volumetric Rates in the Local Universe

In this section, we estimate the volumetric rates of Ca-rich gap transients using the ZTF CLU experiment. As a large-scale systematic and controlled experiment, the volume-limited SN classification effort provides the first direct way to estimate the volumetric rates of this class within 200 Mpc due to its high spectroscopic completeness (≈90%) down to the experiment limiting magnitude of 20 mag.

5.1. Demographics from the Volume-limited Experiment

Since the volume-limited experiment has high spectroscopic classification completeness, a straightforward way to estimate the volumetric rates of Ca-rich gap transients relative to other SNe is to compare the number of events. We perform this analysis by restricting the sample of transients in the CLU experiment to within the volume where Ca-rich gap transients are detectable. Based on the luminosity function of known events discussed in Section 5.2, we find that the average Ca-rich gap transient (peaking at $M = -16$ mag) is detectable out to 150 Mpc for a flux limit of $r = 20.0$ mag, which is the target limiting magnitude of the CLU experiment. Within the experiment duration mentioned above, a total of eight Ca-rich gap transients were detected along with 133 SNe Ia that were classified in the same volume. So, we can place a lower limit on the rates of Ca-rich gap transients of 6% of the volumetric rates of SNe Ia, or 1.5×10^{-6} Mpc^{-3} yr^{-1} (assuming the SN Ia rate is 2.5×10^{-5} Mpc^{-3} yr^{-1}; Frohmaier et al. 2019). Note that this estimate is likely an underestimate of the true rate of Ca-rich gap transients since SNe Ia will be bright in the 150 Mpc volume (peaking at ≈17 mag) and thus detectable during the survey for at least ≈100 days around peak, while the average Ca-rich gap transient in this volume is visible for ≈10–20 days. In addition, our selection criteria require the detection of each source on the rise to peak, which further limits the sample of fast-evolving Ca-rich transients relative to the slow-rising SNe Ia. A true estimate of the volumetric rate of Ca-rich gap transients thus requires a simulation of the cadence of the ZTF survey together with the characteristic luminosity evolution of a Ca-rich gap transient to be able to estimate the number of sources that pass our light-curve selection criteria as a function of the input volumetric rate.

5.2. Luminosity Function

We aim to derive the luminosity function of Ca-rich gap transients using the controlled sample of events from the CLU experiment. Due to the small number of events, we do not separate the spectroscopic subtypes discussed in this work when estimating luminosity functions and volumetric rates. In

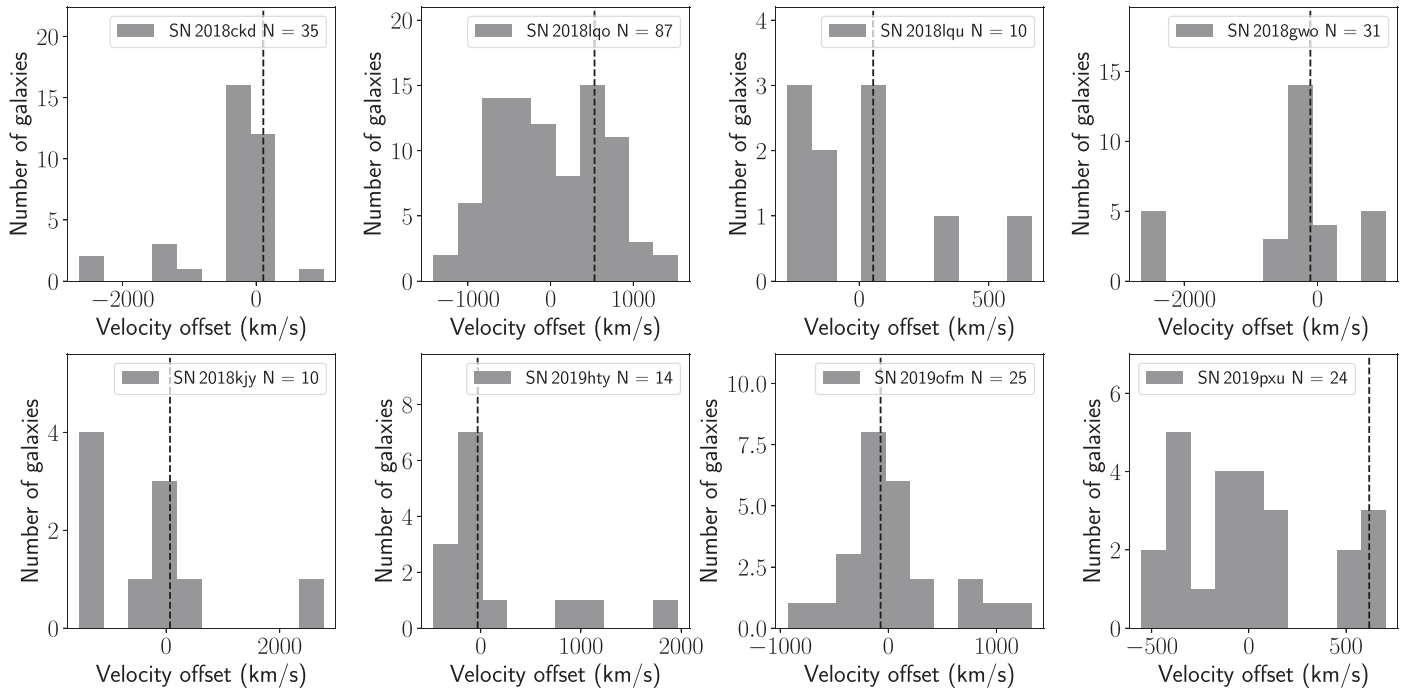

Figure 22. Velocity distributions of galaxies in the environments of the ZTF Ca-rich gap transient sample that have previously known spectroscopic redshifts in the CLU catalog. In each distribution, we define zero velocity as the median of the redshift distribution of all the galaxies in the projected vicinity of the transient, and show the velocity of the assumed (nearest) host galaxy of the transient with a dashed line. The transient name and number of galaxies in each histogram are indicated in the legend.

Figure 23, we show the observed histograms of the peak r-band magnitudes of the literature sample of Ca-rich objects and the ZTF sample of objects. The majority of the literature events exhibit peak magnitudes between $M = -16.5$ mag and $M = -15.5$ mag, while the ZTF sample shows a near-uniform distribution between $M = -17$ mag and $M = -15.5$ mag. However, it is difficult to quantify the selection biases when combining the literature sample of events with the ZTF sample due to the diverse selection criteria of the surveys that detected the literature objects. In order to derive an unbiased luminosity function, we focus specifically on the ZTF sample of events. Despite being classified as part of the CLU experiment, most of the objects in the ZTF sample are not luminous enough to be detectable across the entire experiment volume (200 Mpc) for a limiting magnitude of $r = 20$ mag, and thus volume correction needs to be applied to recover the true luminosity function.

We show a VCLF histogram of the ZTF Ca-rich sample in Figure 23. For each object, we apply a volume correction of $\frac{1}{V_{\rm max}}$, where $V_{\rm max}$ is the maximum volume out to which the object would be detectable for a limiting magnitude of 20. For sources that would be detectable at >200 Mpc, we set the relevant volume to 200 Mpc given the volume-limited nature of the experiment. The VCLF shows evidence of an increasing number of events down to the faintest event, and a simple linear polynomial describes the VCLF well. It is difficult to constrain the luminosity function below the faintest observed events, since it is unclear if there is a population of fainter events which would be detectable only within a very small volume (<100 Mpc). Hence, for the purpose of the simulations, we restrict the observed function between $M = -17$ mag (the upper luminosity limit for our sample) and $M = -15.3$ mag (of the faintest observed event, SN 2012hn). We caution that the ZTF CLU experiment is not sensitive to transients brighter than

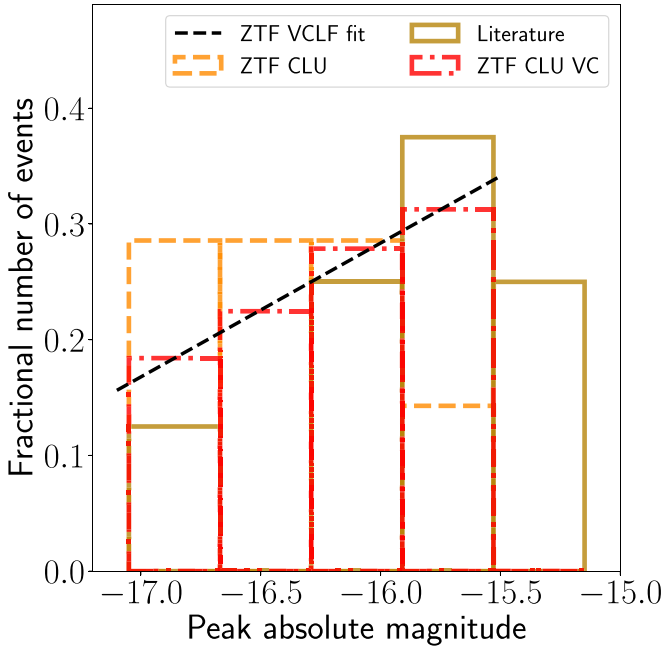

Figure 23. Peak r-band absolute magnitude distribution of the literature sample of Ca-rich gap transients (gold solid) and the ZTF sample (orange dashed). The dotted–dashed distribution in red shows the volume-corrected luminosity function (VCLF) of the ZTF sample, where a $\frac{1}{V_{\rm max}}$ weighting is applied, with $V_{\rm max}$ being the maximum volume out to which the transient would be detected by the volume-limited experiment. The black dashed line shows a linear fit to the VCLF.

$M = -17$ mag at peak due to the sample selection criteria, if such a population exists. Our rate estimates are thus limited to events peaking at $-15.3 > M > -17$.

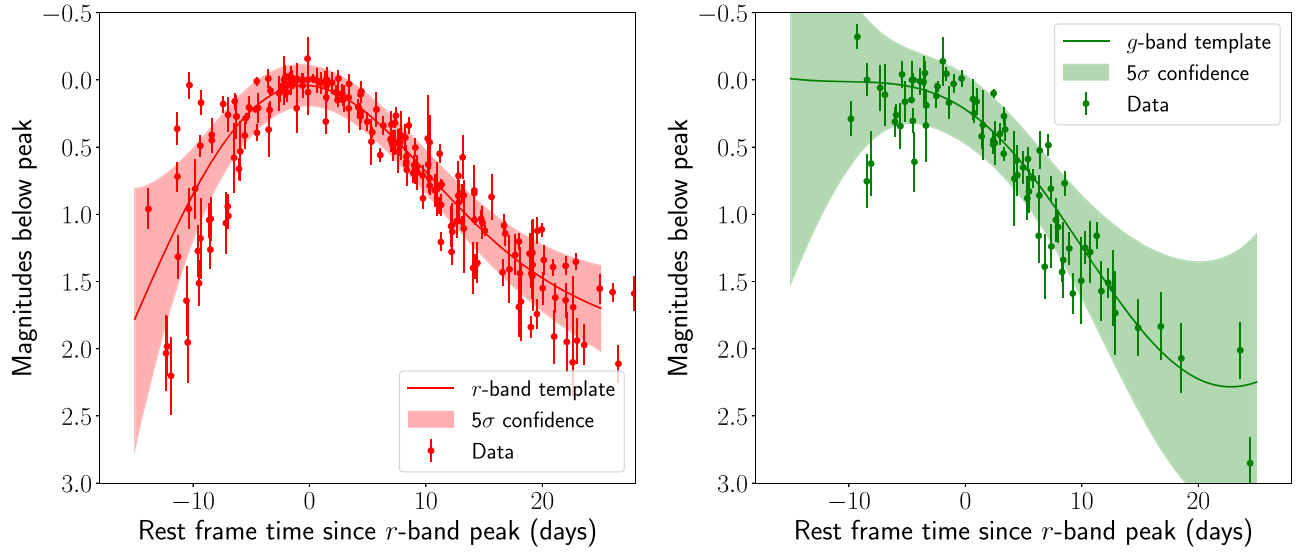

Figure 24. r-band and g-band light-curve templates for Ca-rich gap transients, normalized to peak magnitude. The points with error bars show the observed light curves with 1σ error bars in the respective filters while the solid lines indicate the best-fit light curve from Gaussian process fitting. The shaded regions indicate the uncertainty intervals derived from the Gaussian process fitting, corresponding to 5σ confidence regions.

5.3. Template Light Curve for a Ca-rich Gap Transient

In order to provide a more robust estimate of the volumetric rates of Ca-rich gap transients, accounting for their low-luminosity light curves and the ZTF survey cadence, we start by constructing a template light curve of a Ca-rich gap transient in the r and g bands (which have the most photometric coverage) using the data available for the events in the combined sample. Since we are interested in the photometric evolution timescale of each event, we first normalize each light curve by its peak magnitude measured in the respective filter. Time is measured with respect to the best-fit r-band peak time. We then fit a Gaussian process model with a constant kernel to the normalized light curves in each filter to construct a normalized light-curve template in the r and g filters.

We perform the fit in the phase space of magnitude versus time ranging from -15 days before the r-band peak to $+25$ days after the r-band peak, where there is photometric coverage for more than one object in both filters. This produces the average peak-normalized template light curve and its uncertainty as a function of phase from the r-band maximum. We do not include photometry upper limits in the fit. In Figure 24, we show the peak-normalized data and best-fit templates together with their uncertainties for the two filters. In particular, we note that the sample of peak-normalized light curves in both filters is fairly homogeneous around peak light (even though there is a dispersion in the peak magnitudes), suggesting that a single light-curve template normalized to peak magnitude can well capture the shape of the light curve.

5.4. Simulations of the ZTF Survey

Using the derived luminosity function and light-curve templates for the class of Ca-rich gap transients, we estimate their volumetric rates in the local universe using the `simsurvey` code (Feindt et al. 2019). `simsurvey` is capable of simulating transient light curves as would be observed by ZTF for a given input SN template (provided using the `sncosmo` package from Barbary et al. 2016), and an input survey tiling pattern and duration (termed a survey plan). We use the best-fit r- and g-band templates to construct a `TimeSeriesSource` model in the `sncosmo` package to simulate the spectral evolution of a Ca-rich gap transient between 15 days before and 25 days after the r-band peak. We then use the actual ZTF observing history between 2018 June 1 and 2019 September 30 in any of the public or collaboration surveys as the input survey plan. Since the ZTF reference images were created shortly before the start of the survey and extended well into the time period discussed here for some fields, we only consider pointings that were acquired at least 60 days after the end of reference creation to avoid contamination of the reference images by transient light.

We then simulate the ZTF light curves of the Ca-rich gap transients for a range of input volumetric rates, performing 100 simulations of the ZTF observing plan for each input rate. Based on the observed VCLF, we fix the peak absolute magnitude distribution of the injected transients to a linear function between $M = -15.3$ mag and $M = -17$ mag in the r band. We assume a color of $g - r = 0.7$ mag at the r-band peak (based on the observed color evolution of the sample). Transients are injected out to a redshift of $z = 0.05$. In order to select transient candidates that would have passed the selection criteria defined in this experiment, we perform quality cuts on the simulated light curves as follows:

1. At least two detections of the source are required above an S/N of 5 in either the $g_{\rm ZTF}$ or $r_{\rm ZTF}$ filter.
2. The peak detected magnitude of the transient should be $m < 20$ in either the $g_{\rm ZTF}$ or $r_{\rm ZTF}$ filter.
3. The transient is observed before peak such that there is at least one detection with S/N > 5 before the peak of the light curve in either the $g_{\rm ZTF}$ or $r_{\rm ZTF}$ filter.

Applying these selection criteria to the sample presented in this paper, all but SN 2018gwo, which was recovered after peak light, satisfy the criteria. We use the average number of transients qualifying for these cuts as the best estimate of the number of detected transients for each input volumetric rate, while the standard deviation of the number detected in the simulations is taken as the uncertainty. We show the expected number of detected transients as a function of the input volumetric rate in Figure 25. Figure 25 also shows the fraction

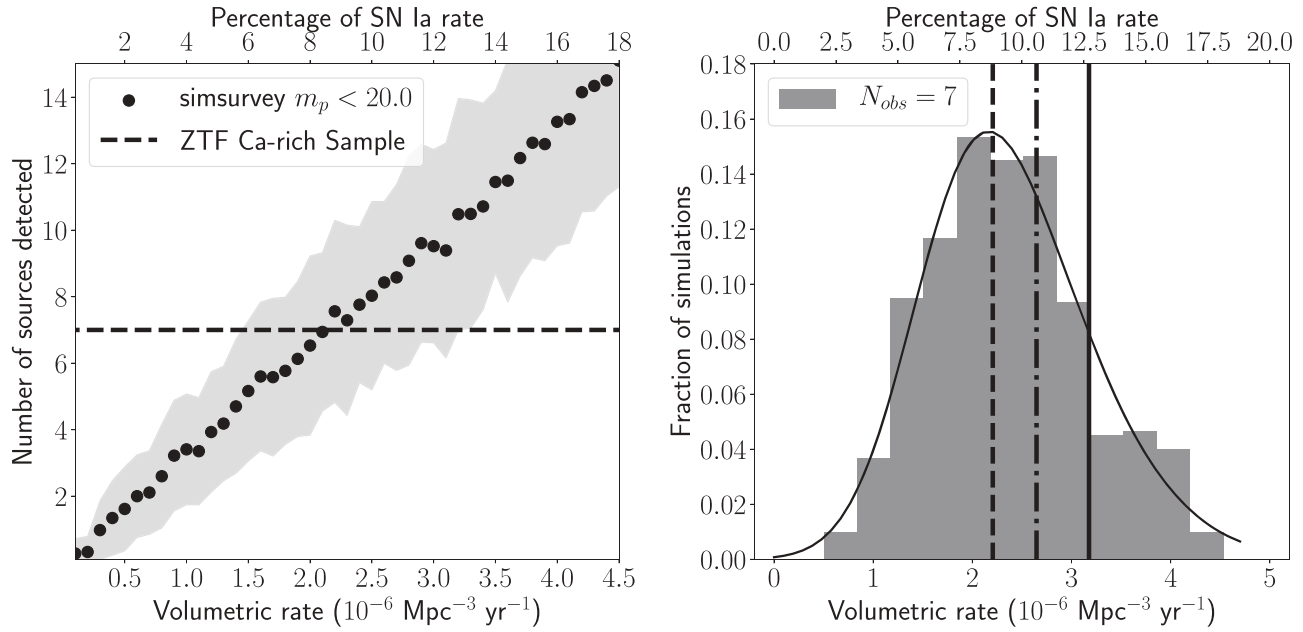

Figure 25. Estimate of the volumetric rate of Ca-rich gap transients with simulations of the ZTF survey using the `simsurvey` code. (Left panel) We show the number of sources passing our selection criteria for the CLU experiment as a function of the input volumetric rate (see text). The points and error bars are the mean and standard deviation of the number of transients recovered as a function of the volumetric rate, while the dashed black line shows the observed number of sources in the experiment. (Right panel) The fraction of simulations producing the observed number of transients as a function of the input volumetric rate. The dependence is fit with a skewed Gaussian distribution shown by the solid line, which we use to derive the best estimate of the volumetric rate and its confidence interval (see text). The dashed line shows the mean of the distribution, the dotted–dashed line shows the rate after correcting for galaxy catalog incompleteness, and the solid line shows the rate estimate after accounting for the transients missed beyond 100″ from their host galaxies.

of simulations that produce the observed number of transients as a function of the input volumetric rate.

Note that `simsurvey` is designed to inject simulated transients over the entire sky for a given input volumetric rate, while the CLU experiment is restricted to transients coincident within 100″ of galaxies with known spectroscopic redshifts. Hence we denote the `simsurvey`-derived rate as $r_{\rm Ca,u,o}$ with the u subscript indicating "uncorrected for the galaxy catalog completeness," and o indicating "uncorrected for offset distribution." The distribution of the fraction of simulations (Figure 25) is well described by a skewed Gaussian function and we fit the fraction of simulations with this functional form to derive the best estimate of the volumetric rate and its 68% confidence interval (similar to the procedure adopted by Frohmaier et al. 2018). We find a volumetric rate of

$$r_{\rm Ca,u,o} = (2.21^{+1.01}_{-0.67}) \times 10^{-6}\,{\rm Mpc^{-3}\,yr^{-1}}. \quad (1)$$

Here, we quote the mode of the probability distribution in Figure 25 as the most likely rate, while the median of the rate probability distribution is 2.40×10^{-6} Mpc^{-3} yr^{-1}. The uncertainty intervals correspond to the central 68% confidence region, bounded by the 15.86 and 84.15 percentiles of the derived distribution. The most likely rate corresponds to $\approx 9^{+4}_{-3}$% of the SN Ia rate in the local universe ($\approx 2.5 \times 10^{-5}$ Mpc^{-3} yr^{-1}; Frohmaier et al. 2019).

In order to estimate the effect of incompleteness of galaxy catalogs in our estimate of the volumetric rate, we use the estimated redshift completeness factor (RCF) from the ZTF BTS (Fremling et al. 2019) as a function of the Wide-field Infrared Survey Explorer W_1 (3.36 μm) magnitude and redshift of the host galaxies. Taking the observed distribution of the redshift z and W_1 absolute AB magnitude M_{W1} (as obtained from the `Tractor` catalogs described in Lang et al. 2016) of the ZTF sample of Ca-rich gap transients, we weight each event by $\frac{1}{{\rm RCF}(M_{W1}, z)}$ for its host galaxy, and sum up over the sample of seven events relevant to the simulation. With this exercise, we find that the incompleteness of galaxy catalogs leads to an underestimation of the Ca-rich gap transient rate by ≈20%. Next, analyzing the full sample of 18 events, we find that 3 out of the 18 objects exhibit offsets larger than 100″ of their host galaxies, although we caution that it is hard to quantify the systematic biases associated with the literature events. Accounting for this effect would increase the inferred rate by another ≈20%. Adjusting for this incompleteness, we derive a rate of

$$r_{\rm Ca} = (3.19^{+1.45}_{-0.96}) \times 10^{-6}\,{\rm Mpc^{-3}\,yr^{-1}} \quad (2)$$

which is 13^{+6}_{-4}% of the volume-averaged SN Ia rate in the local volume.

Owing to the predominance of early-type hosts in this sample, we also compare this rate against the SN Ia rate in early-type galaxies. Li et al. (2011) report a luminosity function averaged SN Ia rate in early-type galaxies of ≈0.05 per 100 yr per 10^{10} $L_{\odot,K}$. Using the local K-band luminosity density in early-type galaxies (Kochanek et al. 2001), we find the corresponding volumetric rate of SNe Ia in early-type galaxies to be $\approx 1.1 \times 10^{-5}$ Mpc^{-3} yr^{-1}. Thus, the inferred rate of Ca-rich gap transients is ≈30% of the volume-averaged SN Ia rate in early-type galaxies. We further note that the rate of SNe Ia in early-type galaxies in cluster environments (Mannucci et al. 2008) is ≈40% lower than the volume-averaged rate per unit mass in Li et al. (2011). This suggests that the rate of Ca-rich gap transients in early-type galaxies in clusters (which is true for nearly all events in our sample) is nearly ≈50% of the SN Ia rate in these environments.

However, we caution that this rate estimate is still strictly a lower limit as we do not include the detection efficiency of the ZTF image subtraction pipeline as a function of transient magnitude and underlying surface brightness. An accurate estimate of the true rate would require us to assign a probabilistic detection likelihood for each simulated detection, using measured detection efficiencies of the ZTF pipeline, which are currently not available. We thus proceed by taking the derived rate as the first measured lower limit to the volumetric rate of Ca-rich gap transients from a large systematic volume-limited experiment.

The derived rate is consistent with those estimated by Perets et al. (2010) from LOSS and Kasliwal et al. (2012) from PTF. Frohmaier et al. (2018) presented the first quantitative analysis of the volumetric rates of Ca-rich gap transients using three events reported by PTF, incorporating the detection efficiency of the PTF pipeline as a function of transient magnitude and background surface brightness. They inferred a rate that could be higher than the rate in this work, of ≈30%–90% of the SN Ia rate in the local universe, although their estimate had large error bars owing to the small number of three events in the PTF sample.

6. Discussion

In this paper, we present observations and analysis of eight new Ca-rich gap transients classified as a part of the ZTF CLU experiment, nearly doubling the sample of known events in the literature. In Section 3 we demonstrate that the ZTF sample shares several similarities to 10 events reported in the literature, while also increasing the diversity of several observed properties among the combined sample. Utilizing the systematic selection criteria of the ZTF sample, we present an analysis of the host environment properties (Section 4) and volumetric rates (Section 5) of the class. In this section, we gather all of these findings to discuss their constraints and implications on the progenitor channels for this class.

6.1. Spectroscopic Subclasses and Correlations

In Section 3, we note the existence of two classes of Ca-rich gap transients distinguished by their spectroscopic appearance at peak—Ca-Ib/c events and Ca-Ia events (see Table 6). We further find a possible continuum of peak light spectral characteristics within the Ca-Ib/c class, wherein the events evolve from green continua with strong P-Cygni features in the blue to events with featureless reddened continua at short ($\lesssim$5500 Å) wavelengths. While the Ca-Ia events are distinguished by their strong Si II features at peak light, we demonstrate a continuum in the peak light spectral features going from Ca-Ia to Ca-Ic to Ca-Ib events. We briefly summarize them here:

1. Ca-Ib/c objects with green continua show strong optical He I features, while events with redder continua show a continuum of strong to weak to no He lines in their peak spectra (Figure 7).
2. He line velocities in red Ca-Ib/c events (≈7000 km s^{-1}) are lower than those observed in green Ca-Ib/c events, which show high photospheric velocities of ≈10,000 km s^{-1}.
3. Red Ca-Ib/c events exhibit slower-evolving light curves (as quantified by $t_{f,1/2}$) compared to green events, with a null hypothesis probability (that the two classes are drawn from the same underlying population of $t_{f,1/2}$) of <5% (Figure 15). This dependence is corroborated by the $g-r$ color dependence of the photometric evolution (Δm_7) shown in Figure 16.
4. Red Ca-Ib/c events typically exhibit lower [Ca II]/[O I] than green Ca-Ib/c events (by a factor of ≈2) at similar phases when the transient spectrum becomes optically thin (Figure 12).
5. Ca-Ia events exhibit more luminous light curves (peak absolute magnitude $M \lesssim -16.5$) than the Ca-Ib/c class, and have red spectroscopic colors/line blanketing and slow photometric evolution similar to those of red Ca-Ib/c events (Figure 15).
6. Although the strong Si II line distinguishes Ca-Ia events from Ca-Ib/c events, there are striking similarities between Ca-Ia and Ca-Ib/c events with redder continua, and we find evidence of a continuum of Si II line strengths going from Ca-Ia to Ca-Ib/c events (Figure 9).

Table 6
Primary Observational Differences between the Ca-Ia and Ca-Ib/c Objects, and Differences between the Green and Red Ca-Ib/c Objects

Observable	Ca-Ia	Ca-Ib/c Red	Ca-Ib/c Green
Si II?	strong	strong to weak	weak
He I?	no	weak to strong	strong
V (10^3 km s^{-1})	6–10 (8)	4–10 (7)	8–12 (10)
Blanketed?	yes	yes	no
M_p (mag)	−16.2–17	−15.3–16.7	−15.5–16.2
Δm_7 (mag)	0.4	0.3	0.5
$g-r$ (mag)	1.0	1.5	0.4
[Ca II]/[O I]	no [O I]	2.5–10 (4)	7–13 (10)

Note. The velocity row is indicated with V, and shows the range of observed peak velocities together with the typical value. The peak magnitude and [Ca II]/[O I] rows show the range of peak absolute magnitudes in the r band and [Ca II]/[O I] respectively.

It is worth noting that even most Ca-Ib/c events exhibit weak but identifiable Si II lines blended with the nearby λ6678 He line (Section 3). We thus find evidence of a sequence in the Ca-rich gap transients going from Ca-Ia to red Ca-Ib/c to green Ca-Ib objects, suggesting a potential continuum of underlying explosion conditions and progenitor systems. We show the corresponding spectroscopic sequence in Figure 26, where we plot the peak light spectra of a few representative members of the Ca-Ia and Ca-Ib/c classes. In addition, we show the peak light spectrum of SN 1991bg (Filippenko et al. 1992), which shows several similarities to the Ca-Ia objects. Thus, the underlying cause of this continuum of spectroscopic appearance could provide a clue to the nature of these explosions. We tabulate and quantify the key observational differences between the different spectroscopic classes in Table 6. We now further this idea of a continuum of underlying progenitor systems as an explanation for the diversity observed in Ca-rich gap transients by probing physical explanations for this continuum.

6.2. Constraints on Ejecta Composition and Mixing

The suppression of flux and features at short wavelengths can be explained as an outcome of line blanketing along the line of sight from Fe-group material in the outer ejecta (e.g., Woosley & Weaver 1994; Nugent et al. 1997). Such features are often seen in peculiar thermonuclear SNe (De et al. 2019b), suggestive of Fe group–rich layers in the outer ejecta. The

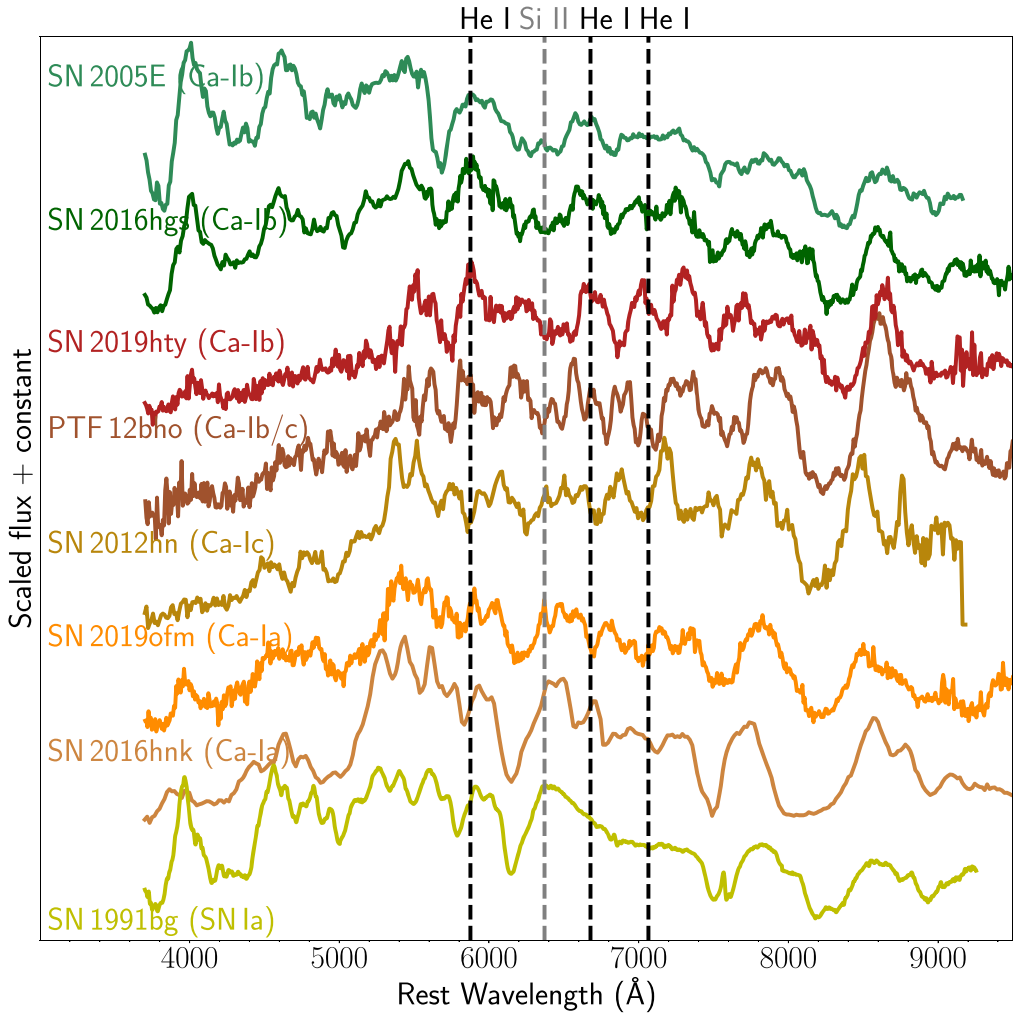

Figure 26. A continuum of spectroscopic and photometric properties in the sample of Ca-rich gap transients. For comparison, we also show the peak light spectrum of SN 1991bg, which shows striking similarities to the Ca-Ia objects. From bottom to top, we find a sequence of events that appear similar to SN Ia 91bg at peak (Ca-Ia events) with strong Si II lines, to SNe Ib/c at peak (Ca-Ib/c events) with weak He lines and line-blanketed continua, and to SNe Ib at peak (Ca-Ib events) with strong optical He I lines and no line blanketing. The colors reflect the photometric colors of the transient at peak. In general, going up the same sequence from bottom to top, the light curves become faster-evolving while the peak $g - r$ colors become bluer. The black dashed lines show the rest wavelength of the optical He I lines and the gray dashed line shows the position of the strong Si II line at ≈6360 Å. Note the increasing depth and higher velocity of the Ca II NIR triplet going from the Ca-Ib to the Ca-Ia events.

presence of such material is expected to produce redder colors in the transient (Nugent et al. 1997; Kromer et al. 2010; Polin et al. 2019a) while increasing the effective opacity of the ejecta due to an increase in bound–bound opacity from the Fe-group material. The increased opacity can also produce slower-evolving light curves if we assume that the underlying ejecta mass distribution is the same (see Figure 17; however, this is not expected to be dominant if the increased opacity is confined only to the outer layers of the ejecta).

The variety in the strengths and velocities of the optical He lines provides yet another clue to the underlying ejecta composition. Due to the high ionization temperature of He, the optical He lines may or may not be excited depending on the ejecta temperature and non-thermal excitation from radioactive material (Lucy 1991). Dessart et al. (2012) show that non-thermal excitation from the radioactive decay of ^{56}Ni is crucial for exciting optical He lines seen in the spectra of SNe Ib/c, thus suggesting that SN Ib/c classification may be related to the amount of ^{56}Ni mixing into the He layer instead of the actual He content of the ejecta (but see also Hachinger et al. 2012). While highly mixed radioactive material in the He layer would produce strong optical He lines, it would also redden the transient color due to the presence of Fe-group material in the outer layers. However, we do not observe this trend in the Ca-rich sample—events with redder continua exhibit weaker (or no) He lines, suggesting a reduction in He content as the amount of Fe-group elements increase in the outer ejecta. In addition, unlike the massive cores in core-collapse SNe, the low optical depth for γ-rays in these low ejecta mass explosions (see De et al. 2018b for a discussion) makes it difficult to hide any non-thermal excitation of He.

While a continuum of Fe-group mass fractions in the outer ejecta appears to explain several of the observables, the reason for the existence of such a continuum remains unclear. This continuum could either be associated with a fundamental transition in the composition of the underlying ejecta, or be due to viewing angle effects. If the outer Fe-group material is produced from He burning in the outer ejecta, one could explain these observations as a continuum of He burning efficiencies in the outer ejecta, wherein the outer ejecta become

richer in Fe-group elements (which cause the line blanketing) as the He burning becomes more complete, thus leading to weaker He lines (see Townsley et al. 2012 for a recent work on the partial burning of He shells).

Nevertheless, it is important to note that the change in peak light continuum properties also appears to affect the appearance of the transient in the late-time nebular phase (its [Ca II]/[O I] ratio) when the ejecta are optically thin and viewing angle effects should be minimal. Both [Ca II] and [O I] are effective coolants of SN ejecta at late times (Fransson & Chevalier 1989) being powered by ^{56}Co decay in the case of normal core-collapse SNe. Together, these observations suggest that cooling in the inner ejecta becomes progressively dominated by [O I] as the outer ejecta become poorer in He content/richer in Fe-group content. Although not discussed thus far, Figure 26 also shows a continuum in the depth and velocity of the prominent Ca II NIR triplet, wherein the absorption becomes deeper and moves to higher velocity over this sequence. Since Ca is a known He burning product (Townsley et al. 2012), this evolution in the Ca II NIR triplet may be associated with the He burning sequence discussed here.

For completeness, we can rule out dust extinction as a possible cause of this evolution—while dust reddening can suppress red continua, it cannot explain the lack of blue-side SN ejecta features seen in the red Ca-Ib/c events. In addition, the remote locations of all of these events and the lack of detectable Na I D absorption in the spectra preclude host galaxy dust extinction.

6.3. Implications for the Explosion Mechanism

6.3.1. Models in the Literature

Shen et al. (2019) summarized the circumstantial evidence used to rule out several progenitor channels in the literature sample based on their environments, hosts, and volumetric rates. Owing to the striking similarities of the host demographics and environments of the ZTF sample and the literature events, our controlled experiment provides corroborating evidence for the preference of these transients for old environments. As in the literature sample, we find core-collapse SNe from massive stars as unlikely progenitor channels due to the prevalence of early-type hosts and large-offset locations with no signs of nearby star formation. On the other hand, the high inferred volumetric rates (lower limit of $\approx$15% of the SN Ia rate) rule out progenitor channels with low expected volumetric rates such as He WD–neutron star mergers, where the field rate is $\sim$100$\times$ lower (Toonen et al. 2018; see also Shen et al. 2019 for arguments against the viability of the high volumetric rates of these systems in globular clusters).

We thus consider the explosive burning of He shells on WDs as the strongest candidates for the cause of these events, and proceed by discussing the implications of our findings on the possible explosion conditions. Assuming that Ca-rich gap transients arise from He shell explosions on WDs, we aim to constrain variations in the underlying progenitor configurations and/or the burning mechanisms using the observed continuum of spectroscopic and photometric properties.

In the He shell detonation scenario, a shell of accreted He on the WD surface (accreted from an He-rich companion) can undergo dynamical burning for large shell masses, and detonate explosively to produce a thermonuclear transient (Iben et al. 1989; Bildsten et al. 2007; Shen & Bildsten 2009; Woosley & Kasen 2011; Sim et al. 2012). Shen et al. (2010) presented calculations of the optical signatures of these events termed ".Ia" SNe, and Perets et al. (2010) suggested that the prototype Ca-rich transient SN 2005E is a result of such a detonation. However, the photometric evolution for the low ejecta mass ($\lesssim$0.2 $M_\odot$) models presented in Shen et al. (2010) is substantially faster than that for SN 2005E, leading Perets et al. (2010) to suggest that more massive shells could explain the slower light-curve evolution.

Waldman et al. (2011) carried out explosive nucleosynthesis calculations of the shell detonation scenario with a 0.2 $M_\odot$ shell on a 0.45 $M_\odot$ CO WD, and demonstrated the nucleosynthesis of a large amount of intermediate-mass elements together with unburned He in the ejecta. Including non-thermal excitation effects, Dessart & Hillier (2015) showed that these events exhibit low-luminosity light curves, He spectroscopic signatures at peak light, and [Ca II] emission in the nebular phase, and are thus consistent with Ca-rich gap transients. Yet, the relatively slow light-curve evolution of most of the literature events requires even more massive shells ($\gtrsim$0.2 $M_\odot$) than these calculations if the underlying core is not detonated. In particular, Dessart & Hillier (2015) showed that the ratio of [Ca II] to [O I] emission depends not only on their relative abundance, but also on where the γ-rays from late-time radioactive decay are being deposited, as these lines are primary coolants of the regions of ejecta where they exist. They further showed that the ejecta continue to cool predominantly through [Ca II] emission even if [O I] is present owing to the higher efficiency of [Ca II] cooling, thus pointing out the importance of the mixing of radioactive material as well as the Ca and O regions in determining [Ca II]/[O I] in the nebular phase (Fransson & Chevalier 1989).

Modifications to this scenario involving the detonation of the underlying CO core and the conditions required therefor have also been explored in the literature, first in the context of double-detonation models for SNe Ia (Nomoto 1980, 1982a, 1982b; Woosley et al. 1986; Woosley & Weaver 1994; Livne & Arnett 1995). These initial models invoked thick He shells ($\sim$0.1 $M_\odot$) for this scenario and were largely ruled out due to the predicted red colors and strong line blanketing signatures found for these configurations (e.g., Nugent et al. 1997).

Later studies found that thin He shells (as low as 0.01 $M_\odot$) on relatively massive CO cores ($\gtrsim$0.8 $M_\odot$) can detonate the underlying WD (Bildsten et al. 2007; Fink et al. 2010; Shen et al. 2010; Shen & Moore 2014), potentially producing luminous slow-evolving transients akin to normal and sub-luminous SNe Ia (Kromer et al. 2010; Sim et al. 2010; Woosley & Kasen 2011; Polin et al. 2019a). Specifically, the slower-evolving light curves in these models may be consistent with Ca-rich gap transients; however, since the luminosity and timescale of these light curves increase with the underlying total mass (owing to higher Ni production from higher-density cores), Ca-rich gap transients are likely associated with explosions on lower-mass WDs in this scenario.

To this end, Sim et al. (2012) further extended these calculations to lowest-mass CO WDs ($\approx$0.45 $M_\odot$) with thick He shells (0.2 $M_\odot$) specifically to probe the parameter space for subluminous and fast-evolving events like Ca-rich events. They found that secondary detonations are likely triggered for these shell masses (although there remain large uncertainties), and presented a suite of simulations varying the extent and

mechanism of the core detonation to demonstrate the corresponding effects on the nucleosynthetic signatures. They specifically noted that their suite of models produced transients brighter (peak absolute magnitude $\lesssim -17$) than the prototype SN 2005E, and thus reproducing the properties would require lower yields of radioactive material that could be possible in lower-density He shells (Shen & Bildsten 2009; Woosley & Kasen 2011) or via significant pollution of the shell with C (Kromer et al. 2010).

6.3.2. Ca-rich Gap Transients from He Shell Explosions

Jacobson-Galán et al. (2020) suggested that the Ca-Ia object SN 2016hnk is consistent with the detonation of a thin ($\approx$0.02 $M_\odot$) He shell on a $\approx$0.8 $M_\odot$ WD. This interpretation is based on recent work by Polin et al. (2019b) showing that the ejecta in double-detonation events could cool predominantly through [Ca II] lines in the nebular phase (instead of Fe-group lines as in other SNe Ia) for low total (WD core + He shell) masses ($\lesssim$0.9 $M_\odot$), even if the Ca abundance in the ejecta is of the order of a few percent. This channel thus provides a promising scenario to explain the origins of Ca-Ia objects, owing to their luminous and slow-evolving light curves, strong line blanketing signatures with SN Ia–like spectra, and [Ca II] emission in the nebular phase. The observed diversity in the peak luminosities could then be associated with a range of WD core masses.

Therefore, it is interesting to extend this mechanism to a continuum of He shell and CO core masses, which may explain the diversity in the population of Ca-Ib/c events with double detonations. Unlike pure shell detonations, which cannot fully explain the relatively slow-evolving light curves of prototypical Ca-rich transients like SN 2005E and SN 2010et (see, for example, Waldman et al. 2011 and Dessart & Hillier 2015), double detonations predict slower-evolving light curves compared to pure shell detonations due to the higher ejecta mass involved (Woosley & Kasen 2011; Sim et al. 2012). Considering that SN 2005E and SN 2010et belong to the class of green Ca-Ib/c events, which have faster-evolving light curves, the problem of slow evolution is even worse for red Ca-Ib/c events, which exhibit slower light curves similar to Ca-Ia events (Figure 15), leading us to consider double detonations for the red Ca-Ib/c events.

Owing to the explosive burning of He-rich material, a common spectroscopic prediction of the He shell double-detonation scenario is a transient marked by strong line blanketing features of Fe-group material and Ti II (at early times when the photosphere is in the He detonation material), in addition to intermediate-mass elements produced from the core burning (Hoeflich & Khokhlov 1996; Nugent et al. 1997; Kromer et al. 2010; Woosley & Kasen 2011; Polin et al. 2019a; Holcomb et al. 2013). Such signatures are also found in pure shell and double detonations on lower-mass WDs (Dessart & Hillier 2015; Sim et al. 2012). While previous attempts to model green Ca-Ib/c objects (Dessart & Hillier 2015; Sim et al. 2012) have had difficulty accounting for the relatively blue colors of these transients at peak, the red colors, line blanketing, and slow evolution make the double-detonation channel an attractive possibility for red Ca-Ib/c events. The typically lower peak luminosity of red Ca-Ib/c events would then require detonations on lower-mass WDs compared to Ca-Ia events.

However, despite having unburned He in the ejecta (Townsley et al. 2012; Sim et al. 2012; Moore et al. 2013; Polin et al. 2019a), existing works on double detonations do not demonstrate whether He I lines can be reproduced as observed. On the other hand, Si II lines are the most conspicuous spectral features in these models as seen in Ca-Ia objects. Red Ca-Ib/c events show weak but clear signatures of He, sometimes stronger than the Si II lines. We note that existing models have primarily explored this scenario with relatively higher-mass WDs ($\gtrsim$0.8 $M_\odot$), and without including the non-thermal radiation effects required to excite He lines (Sim et al. 2012 explored lower-mass WDs but without non-thermal effects). Given the continuum of strong to weak He lines observed in the red Ca-Ib/c population, it is possible that these explosions constitute a range of shell burning efficiencies, and correspondingly He content in the ejecta depending on the pressure at the base of the shell at the time of ignition (Moore et al. 2013). Ca-Ia events would then represent the extreme end of this population where He is nearly completely burned to Fe-group elements.

In the nebular phase, red Ca-Ib/c objects often show strong [O I] emission, unlike Ca-Ia events. If both red Ca-Ib/c events and Ca-Ia events arise from double detonations but with different underlying WD masses, this provides observational evidence that core burning becomes less efficient as one moves toward smaller core masses. A possible explanation is core detonation transitioning from converging shock detonations in high-mass cores to edge-lit detonations (Nomoto 1982b; Livne & Glasner 1990, 1991) at the base of the shell for lower-mass WDs. Owing to the lower density of the core in edge-lit detonations, Sim et al. (2012) show that these explosions produce incomplete burning of the core (and thus lower Ni yields and fainter light curves) and larger amounts of O in the core, both consistent with the red Ca-Ib/c population. Alternatively, it is possible that a larger fraction of the Ni produced in the core detonation is convectively mixed into the O-rich regions of the ejecta for lower-mass WD cores, thus producing stronger [O I] emission in the nebular phase.

Ca-Ib/c objects with green continua pose several problems to the general double-detonation picture above, especially with regard to their bluer colors at peak without line blanketing signatures. The lack of these signatures suggests a scenario where the outer ejecta is not significantly enriched with Fe-group elements, while the strong He line signatures indicate low He burning efficiency. Taken together with their systematically faster-evolving light curves, these signatures likely point to a low-efficiency burning mechanism that ejects a small amount of material. Although pure He shell detonation scenarios also predict line-blanketed spectra (due to the abundance of Ti II near the photosphere; e.g., Waldman et al. 2011; Dessart & Hillier 2015), lower He burning efficiency has been shown to be achievable if the pressure at the base of the shell is lower (Perets et al. 2010; Moore et al. 2013). If so, the higher photospheric velocities, relatively fast photometric evolution, and weak [O I] emission in the nebular phase are consistent with the properties of green Ca Ib/c events (Waldman et al. 2011; Dessart & Hillier 2015). The relatively low peak luminosity of this group (Table 6) then translates to a lower amount of radioactive material synthesized in these shell-only explosions compared to double detonations.

Alternatively, such low-efficiency burning conditions may be achieved in pure shell deflagrations. The study of this mechanism is extremely limited at this time but Woosley & Kasen (2011) show that these explosions produce slowly

evolving subluminous light curves, but with low photospheric velocities ($\approx$4000 km s^{-1}). However, that study was performed with 1D simulations, which are poorly suited for deflagrations, and future work is required to determine if higher velocities could be achieved to make this a plausible scenario.

We note that early excess emission has so far been clearly seen only in the green Ca-Ib/c objects SN 2016hgs and SN 2018lqo. If these explosions are indeed associated with He shell detonations or deflagrations, these observations suggest that the outer ejecta produced in the shell burning is enriched with short-lived isotopes (e.g., ^{48}Cr, ^{52}Fe, and ^{56}Ni with half-lives of 0.90 days, 0.35 days, and 6.07 days respectively), as has been found in previous simulations of the pure shell detonation scenario (Shen et al. 2010). Although the early bump in iPTF 16hgs is potentially consistent with a core-collapse explosion from a giant He star (e.g., Woosley 2019), the detection of this bump in SN 2018lqo in an old elliptical galaxy strongly precludes a core-collapse interpretation. Although most objects in the green Ca-Ib/c sample do not have well-sampled early-time light curves to detect this early emission, this phenomenon is clearly not ubiquitous in the Ca-Ib objects as demonstrated by the monotonic rise observed in the well-sampled early light curve of SN 2010et (Figure 13).

6.4. Implications for the Progenitor Stellar Populations

We have thus far discussed the implications of diversity in the photometric and spectroscopic properties of the Ca-rich gap transient population for the underlying explosion mechanism. Broadly, we find that the range of observed properties can be explained with scenarios involving explosive He burning on the surface of a CO WD. Specifically, the slowly evolving light curves of the Ca-Ia and red Ca-Ib/c objects are difficult to explain using scenarios involving pure shell detonations, and likely require relatively massive explosions that detonate the underlying core. On the other hand, the green Ca-Ib/c objects may be consistent with shell-only explosions with low He burning efficiency. We now extend this discussion to probe the implications of the environments of these transients for the inferred progenitors, i.e., WDs accreting He from a companion. As noted in several previous works, this population of transients is distinguished from other classes by a striking preference for large offsets from their passive host galaxies in predominantly group and cluster environments. These two trends generally point to old stellar populations with long delay times, and preclude channels that have a significant rate at short delay times ($\lesssim$1 Gyr; Perets et al. 2010; Meng & Han 2015). We note that several objects in our combined sample (iPTF 16hgs, SN 2016hnk, and SN 2019ofm) are found in star-forming environments, suggesting that there is a small but likely non-zero contribution at short delay times as well.

The pathways of stellar evolution to explosive burning of He shells have been explored in several previous works (Nomoto 1982a; Woosley & Weaver 1994; Bildsten et al. 2007; Shen & Bildsten 2009; Brooks et al. 2015; Bauer et al. 2017), with tight B-type subdwarf + WD systems (Geier et al. 2013; Kupfer et al. 2017) and AM Canum Venaticorum (AM-CVn) binaries (Nelemans et al. 2004) being possible well-observed evolutionary stages prior to the detonation. The observed formation rate of stable accreting AM-CVn systems in the Milky Way is $\sim 1.3 \times 10^{-4}$ yr^{-1} (Roelofs et al. 2007; Carter et al. 2013) or $\sim$2% of the SN Ia rate in Milky Way–like galaxies (Li et al. 2011). Bildsten et al. (2007) used this to estimate the rate of He shell detonations to be 2%–6% of the SN Ia rate in E/S0 galaxies assuming all AM-CVns detonate in a last flash. This rate is $\approx$3–7$\times$ lower than our lower-limit estimate for the volumetric rate of Ca-rich gap transients, and is thus likely to be inconsistent. However, we cannot rule out the scenario where the green Ca-Ib events of the Ca-rich continuum discussed here originate in these explosions.

Similar detonation conditions can also be achieved in the case of mergers of He WDs with CO WDs (e.g., Pakmor et al. 2013), where a variety of detonation conditions could be achieved depending on how the He layer settles on the surface of the more massive WD (Fryer et al. 2010; Dessart & Hillier 2015). The merger rate of He + CO WD binaries in the field for a Milky Way–like galaxy is $\sim 3 \times 10^{-3}$ yr^{-1} (Brown et al. 2016) or $\approx$10% of the SN Ia rate, suggesting that most He + CO WD binaries end up merging to produce thermonuclear transients or stable long-lived remnants (e.g., R Coronae Borealis stars; Clayton 1996; Schwab 2019). The high rate of these mergers within Milky Way–like galaxies is however in contradiction with the preference for large-offset distributions (long delay times) of the Ca-rich gap transient population (Shen et al. 2019). The measured rate in the halo (Brown et al. 2016) is only $\sim$10% of the rate within the galaxy ($\sim$1% of the SN Ia rate) and hence inconsistent with our estimates for the Ca-rich transients that reside in or outside their host halos.

With population synthesis calculations, Meng & Han (2015) suggested that the relatively high rates and long delay times of the Ca-rich gap transient population could be consistent with double-WD binaries with a CO WD $\lesssim$0.6 $M_\odot$ and an He WD $\lesssim$0.25 $M_\odot$, specifically highlighting the low mass as a key aspect of the delay time extension. This is consistent with our suggestion of low-mass WDs being the progenitor population, but the observed halo population of He–CO WD mergers remains too rare to explain the high rate (Brown et al. 2016). The measured rates are high enough such that there is one Ca-rich gap transient for every three SNe Ia in early-type galaxies, suggesting that the progenitors must be nearly as common as the progenitors of SNe Ia.

Together, we find that the observed merger rates of WDs in He-rich accreting systems are too low in the field in the outskirts of galaxies to explain the high rates of Ca-rich gap transients. However, the interaction rate may be enhanced in dense stellar systems like globular clusters (see, e.g., Pfahl et al. 2009; Samsing et al. 2017). Although such stellar systems are not detected exactly at the positions of known Ca-rich gap transients (Lyman et al. 2014, 2016; Lunnan et al. 2017), Shen et al. (2019) suggest these transients could be produced from being kicked out due to dynamical interactions inside dense stellar systems in the outskirts. Yuan et al. (2013) and Shen et al. (2019) argue that the locations and host environments are consistent with the globular cluster scenario; however, we continue to find that the number of Ca-rich gap transients at small offsets is too small compared to the globular cluster offset distribution in Shen et al. (2019). Additionally, the preference for rich cluster environments is even more extreme than that for globular clusters and remains to be explained.

Based on our deep late-time imaging observations of the transient locations, we find in four out of eight cases evidence of faint and diffuse nearby or underlying stellar associations. We estimate the absolute magnitudes of these sources to be ≈ -9 mag to -11 mag at the redshift of the transient. A similar diffuse system was also detected in late-time imaging of

PTF 11kmb (Lunnan et al. 2017). While we caution that the chance coincidence probability of background galaxies at this depth is high, we speculate about the implications of these being associated with the transient itself. Specifically, a population of such faint and ultra-diffuse galaxies have been detected in low surface brightness imaging surveys (Abraham & van Dokkum 2014) in nearby clusters. These systems appear to exhibit an overabundance (by nearly an order of magnitude) of globular clusters as compared to the expected numbers for their luminosity (van Dokkum et al. 2017, 2016, 2018). Although work remains to be done to constrain the formation rate of double-WD binaries in such dense stellar systems, it is an intriguing possibility that the offset locations of Ca-rich gap transients may be due to an overabundance of globular clusters in ultra-diffuse galaxies within nearby galaxy groups and clusters.

While Shen et al. (2019) point out that a relatively large fraction of WDs in globular clusters could be required to explain the estimated rate in Frohmaier et al. (2018), our lower rate estimates may provide a more viable solution to the problem. The locations of these transients in early-type galaxies in predominantly rich cluster environments are indeed suggestive given that up to 30%–70% of stellar light may be in intra-cluster light in these environments (D'Souza et al. 2014; Perets 2014).

7. Summary

In this paper, we present the design and completeness of the CLU experiment of the ZTF, aimed at assembling a spectroscopically complete sample of transients in the local universe within 200 Mpc. With a total sample of 754 spectroscopically classified SNe, we present the first systematic search for Ca-rich gap transients. Using simple and systematic selection criteria, we identify a sample of 22 low-luminosity hydrogen-poor SNe as candidate Ca-rich gap transients from the first 16 months of operations, which are followed up with nebular-phase spectroscopy. We report the detection of eight Ca-rich gap transients in this sample, which we combine with the literature sample of 10 events that pass the same selection criteria. We perform the first systematic study of the spectroscopic and photometric properties of this sample and identify several trends and correlations that have implications for the underlying explosions and progenitor systems. Summarizing these correlations, we find the following:

1. Ca-rich gap transients broadly bifurcate into two classes based on their peak light spectroscopic similarity to SNe Ia (with strong Si II lines; Ca-Ia objects) and SNe Ib/c (without strong Si II lines; Ca-Ib/c objects).
2. Ca-Ib/c objects show a bimodal population in peak light spectral properties based on their spectroscopic behavior blueward of ≈5500 Å, wherein some events exhibit red continua and strong line blanketing of blue flux (Ca-Ib/c-red) while other events exhibit flat continua with clear P-Cygni absorption features of metals at short wavelengths (Ca-Ib/c-green). Ca-Ia objects always show line-blanketed spectra at peak.
3. Ca-Ia objects do not show any He lines, red Ca-Ib/c objects show a continuum from weak to strong He lines (velocity ≈ 7000 km s^{-1}), and green Ca-Ib/c objects always exhibit strong He lines at higher velocities of ≈10,000 km s^{-1}.
4. Photometrically, red Ca-Ib/c events with line blanketing signatures exhibit redder colors at peak and slower-evolving light curves ($\Delta m_7 \approx 0.3$ mag) compared to green Ca-Ib/c events ($\Delta m_7 \approx 0.5$ mag), where Δm_7 is the decay of the r-band light curve in 7 days from peak light. Ca-Ia events also exhibit relatively slow photometric evolution compared to green Ca-Ib/c objects ($\Delta m_7 \approx 0.4$ mag).
5. Ca-Ia objects do not show [O I] in the nebular phase, while red Ca-Ib/c objects show stronger [O I] lines in the nebular phase relative to [Ca II] and green Ca-Ib/c objects show weaker [O I] lines (higher [Ca II]/[O I] flux ratios) relative to red Ca-Ib/c objects.
6. We find tentative evidence of a spectroscopic continuum of properties going from Ca-Ia to Ca-Ic to Ca-Ib objects, where Si II lines get weaker, He I lines get stronger, and line blanketing becomes less significant in the spectrum in moving along that sequence. Photometrically, the peak light colors get bluer while the light-curve evolution becomes faster along this sequence.

We find that these spectroscopic properties and the corresponding trends can be broadly explained in scenarios involving the explosive burning of He shells on low-mass WDs ($\lesssim$0.8 $M_\odot$). The slowly evolving light curves and line-blanketed spectra of the Ca-Ia and red Ca-Ib/c events are consistent with scenarios involving the double detonation of He shells on low-mass WDs, where the efficiency of He burning in the outer ejecta is high. On the other hand, the strong He lines, higher velocities, and faster-evolving light curves of the green Ca-Ib/c events suggest lower ejecta mass explosions likely involving He shell–only detonations with low He burning efficiency or even deflagrations. While theoretical modeling of He shell explosions on low-mass WDs remains limited at this time, this data set together with the inferred correlations from the first systematic search for these explosions will be a useful benchmark for future modeling efforts.

The host environments of the sample are dominated by remote locations in the far outskirts of galaxies similar to what was found in previous studies, while the offset distribution is skewed toward large host offsets compared to that of globular clusters. The apparent host galaxies themselves are always found in rich group and cluster environments, and are likely an important clue to the progenitor channels. Using the systematic selection strategy of the experiment, together with the measured incompleteness of galaxy catalogs from the ZTF BTS, we infer the volumetric rates of these events to be at least ≈15% ± 5% of the local SN Ia rate. While the explosion scenarios require WDs with He-rich donors, the observed rates of these systems are apparently too low in the field to explain their high volumetric rates. However, we note that the observed environments of these events in the outskirts of early-type galaxies in clusters are strikingly different from the Galactic disk. We speculate that the rich host environments, offset locations, and faint nearby diffuse stellar associations in some events may point to a contribution from dynamical interactions within ultra-diffuse stellar associations in galaxy clusters, which are found to be extremely rich in globular clusters (van Dokkum et al. 2016, 2017).

Our findings have broader implications for the population of thermonuclear SNe in the local universe. While the double-detonation scenario has been long proposed as a viable explosion-triggering mechanism for SNe Ia, the strong line